Raman Spectroscopy of Single Wall Carbon Nanotubes

by

Hyungbin Son

Submitted to the Department of Electrical Engineering and Computer Science

in Partial Fulfillment of the Requirements for the degree of

Doctor of Philosophy

at the Massachusetts Institute of Technology

June 2008

Author .....
Department of Electrical Engineering and Computer Science
May 2, 2008

Certified by .....
Jing Kong
Assistant Professor of Electrical Engineering and Computer Science
Thesis Supervisor

Certified by .....
Mildred S. Dresselhaus
Institute Professor of Electrical Engineering and Physics
Thesis Supervisor

Certified by .....
Pablo Jarillo-Herrero
Assistant Professor of Physics
Thesis Supervisor

Accepted by .....
Terry P. Orlando
Professor of Electrical Engineering and Computer Science
Chairman, Department Committee on Graduate Thesis

Raman Spectroscopy of Single Wall Carbon Nanotubes

by

Hyungbin Son

Submitted to the
Department of Electrical Engineering and Computer Science

May 2, 2008

in Partial Fulfillment of the Requirements for the degree of
Doctor of Philosophy

ABSTRACT

A single wall carbon nanotube (SWNT) is a new form of carbon, whose atomic arrangement is equivalent to a graphene sheet rolled into a cylinder in a seamless way. The typical diameter of a SWNT ranges from 0.6 nm to several nm and the typical length ranges from tens of nm to several cm. Due to its small diameter and high aspect ratio, a SWNT has very unique electronic and vibrational properties.

The goals of this thesis work are to design and construct a Raman instrument capable of obtaining signals from many different types of individual SWNTs, to develop methods and tools to collect, organize and analyze large amounts of Raman spectra from them, to use resonant Raman spectroscopy to characterize individual SWNTs, and to investigate how their electronic and vibrational properties change under various conditions, such as strain, or different substrate interactions. A high-efficiency widely-tunable Raman instrument is developed for the study of SWNTs. The environmental effects on the electronic and vibrational properties are investigated by suspended SWNTs. Using the high-efficiency Raman instrument, weak optical transitions of metallic SWNTs are found. The effect of strain on the vibrational mode frequencies of SWNTs are studied.

Thesis Supervisor: Jing Kong
Title: Assistant Professor of Electrical Engineering and Computer Science

Thesis Supervisor: Mildred S. Dresselhaus
Title: Institute Professor of Electrical Engineering and Physics

Thesis Supervisor: Pablo Jarillo-Herrero
Title: Assistant Professor of Physics

Acknowledgments

First of all, I shall thank my advisors Professor Jing Kong and Professor Mildred S. Dresselhaus. Prof. Kong was very kind and was willing to listen to students. The family-like atmosphere in her group probably has not been possible without her. Such an atmosphere made my graduate life quite enjoyable. Furthermore, she trusted and supported me when I was initiating risky projects in the early years of my graduate career. Prof. Dresselhaus has been my advisor for seven years since I was a sophomore. During this period I had invaluable lessens from her dedication to science, her way of reasoning, and her social skills. Now I look back, I realize how lucky I was to have her as my advisor. I am also grateful to Professor Pablo Jarillo-Herrero for gladly joining my thesis committee.

I wish to express my special thanks to Ramachandra R. Dasari, the director of MIT spectroscopy laboratory. It would not be possible to list all his support in this page. To mention a few, he provided me with dedicated laboratory space, many lasers, optics training, new projects, collaborators, and so on.

I shall thank my group members, Gene Dresselhaus, Aurea Zare, Xiaoting Jia, Yaping Hsieh, Ming Tang, Federico Villalpando, Mario Hofmann, Daniel Nezich, Hootan Farhat, Alfonso Reina Cecco, and Kyeong-Jae Lee. Everyone was friendly, inspiring and supportive. I also had great time when we had group activities, both inside and outside the lab. They were more like friends to me than just groupmates.

I wish to thank my parents and my sister in Korea for their support and patience during my eight years of study on the opposite side of the globe from home.

Finally, I thank my fiancee Jyewon in Korea for her patience and love. Despite the fact that I can visit Korea only a couple of times a year, she has stayed me until now.

I acknowledge support under NSF Grants DMR-01-16041, DMR-07-04197, INT 00-00408, the Intel Higher Education Program, and the MSD Focus Center, one of five research centers funded under the Focus Center Research Program and a Semiconductor Corporation program. I also thank Xerox MIT fellowship program

for supporting my study during the last year of my Ph. D. program and, especially, Kock-Yee Law, the Xerox sponsor, for sharing interesting ideas with me.

This work made use of MRSEC Shared Facilities supported by the National Science Foundation under Award Number DMR-0213282 and NSF Laser Facility grant #CHE-011370. This work was also carried out using the Raman facility in the Spectroscopy Laboratory supported by NSF CHE 0111370 and by NIH RR02594 grants.

Contents

Chapter 1

Introduction

1.1 Single Wall Carbon Nanotubes

A single wall carbon nanotube (SWNT) is a new form of carbon, whose atomic arrangement is equivalent to a graphene sheet rolled into a cylinder in a seamless way (see Fig. 1-1).[1] The typical diameter of a SWNT ranges from 0.6nm to several nm and the typical length ranges from tens of nm to several cm. Due to its small diameter and high aspect ratio, a SWNT behaves as a one-dimensional system. In other words, the diameter of a SWNT is so small that the quantum confinement in the circumferential direction causes the energy separation between neighboring electronic subbands to be significantly greater than the thermal energy at room temperature.

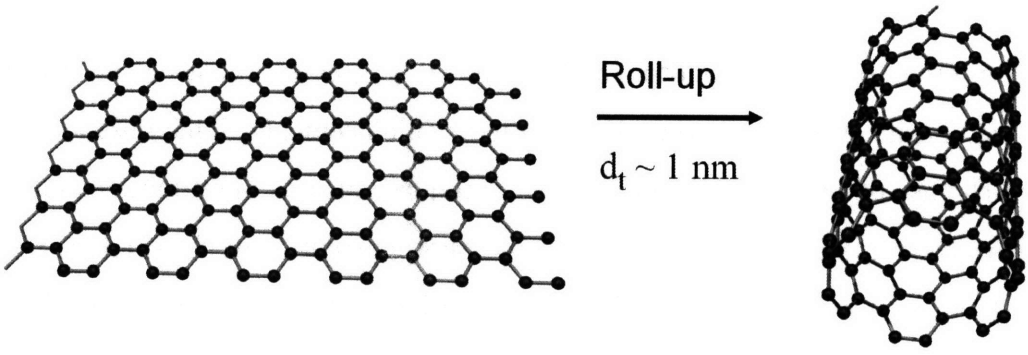

Figure 1-1: A SWNT rolled up from a graphene sheet. d_t denotes the diameter of the SWNT.

Because of the one dimensionality of SWNTs, there exist singularities in the electronic density of states, called van Hove singularities (vHS). The electronic band structure is determined by the geometric configuration of the SWNT. The band gap can be varied by changing the geometric configuration to make the nanotube either metallic or semiconducting. In the case of a semiconducting SWNT, the band gap corresponds to the energy gap between the two vHSs in the valence and conduction bands closest to the Fermi level.

The geometric configuration of the SWNT can be understood by looking at how a graphene sheet is rolled into the SWNT, specifically by looking at the vector that corresponds to the circumference of the SWNT (see Fig. 1-2).[1] This vector, which is called the chiral vector, can be written as the following:

$$C_h = n\mathbf{a_1} + m\mathbf{a_2}, \tag{1.1}$$

where $\mathbf{a_1}$ and $\mathbf{a_2}$ are the two lattice vectors of the graphene sheet and n and m are positive integers ($n \geq m$). The set of numbers (n, m) uniquely identifies the geometric configuration or the chirality of the SWNT. Therefore, each SWNT with different chiral indices (n, m) has a unique electronic and phonon band structure.

1.2 Raman Spectroscopy of Single Wall Carbon Nanotubes

The interaction between a photon and a SWNT is greatly enhanced by the high electronic density of states at the vHS (resonant enhancement). This interaction has enabled the use of various optical probing techniques, such as photoluminescence [2], Raman scattering, Rayleigh scattering [3], and photocurrent [4] at the single nanotube level, which have been used to probe the electronic and vibrational properties of a SWNT. Raman scattering can be particularly useful, since it directly probes many interesting vibrational modes of a SWNT. First of all, the radial breathing mode (RBM) gives a good estimate of the diameter of a SWNT. The G-band, named after

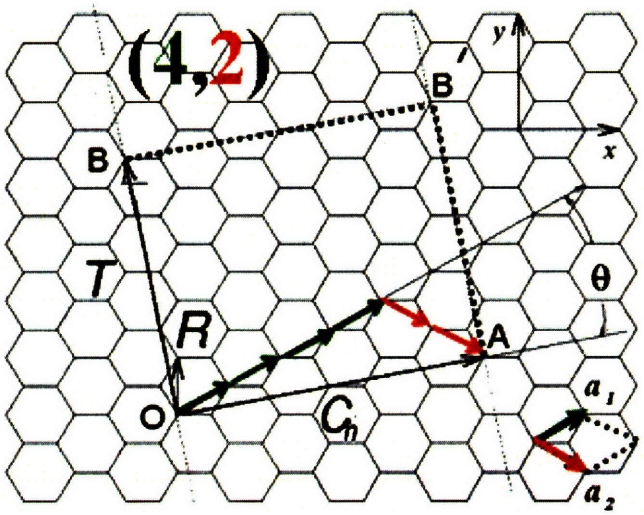

Figure 1-2: The graphene sheet that results from unrolling a SWNT by cutting the cylinder wall of the SWNT parallel to its axis. a_1 and a_2 correspond to the lattice vectors of graphene. $\overline{OA}$ corresponds to the chiral vector and $\overline{OB}$ and $\overline{AB'}$ correspond to the unit translational vector along the tube axis.

the mother material graphite, can be used to probe the temperature, and the presence of the strain or charge transfer of a SWNT. The D-band, as one may imagine from its name, the disorder-induced band, is an indicator of the defectiveness of any graphite-based material, including a SWNT.

However, the Raman scattering experiment at the single molecule level faces a big challenge. While the resonant enhancement enables the study of the interaction between photons and a SWNT at the single nanotube level, when the energy of the photons does not match with the electronic transition energies E_{ii} (which corresponds to the energy difference between the ith vHS peaks in the conduction and valence band) of a SWNT, no significant interaction occurs, rendering optical probing of the SWNT exceedingly difficult.

Since every different (n, m) SWNT has a different electronic band structure and different electronic transition energies E_{ii}, one needs a widely tunable Raman instrument to study different SWNTs. These resonant energies for different (n, m) SWNTs are commonly summarized in the so-called Kataura-plot, in which the E_{ii} values are plotted versus the RBM frequency.[5, 6] Figure 1-3 shows such a Kataura plot.[7]

The blue circles and red squares represent the semiconducting and metallic SWNTs, respectively. The pairs of numbers in parenthesis shown next to the dots are the (n, m) chiral indices. The SWNTs with the same so-called $2n + m$ 'family number' are connected with blue and red solid lines and the family numbers are also shown in Fig. 1-3. From the Kataura plot, one can learn that, to study most (n, m) species with Raman spectroscopy, one needs a Raman instrument that is capable of tuning laser excitation energies between 1.4 eV-2.7 eV.

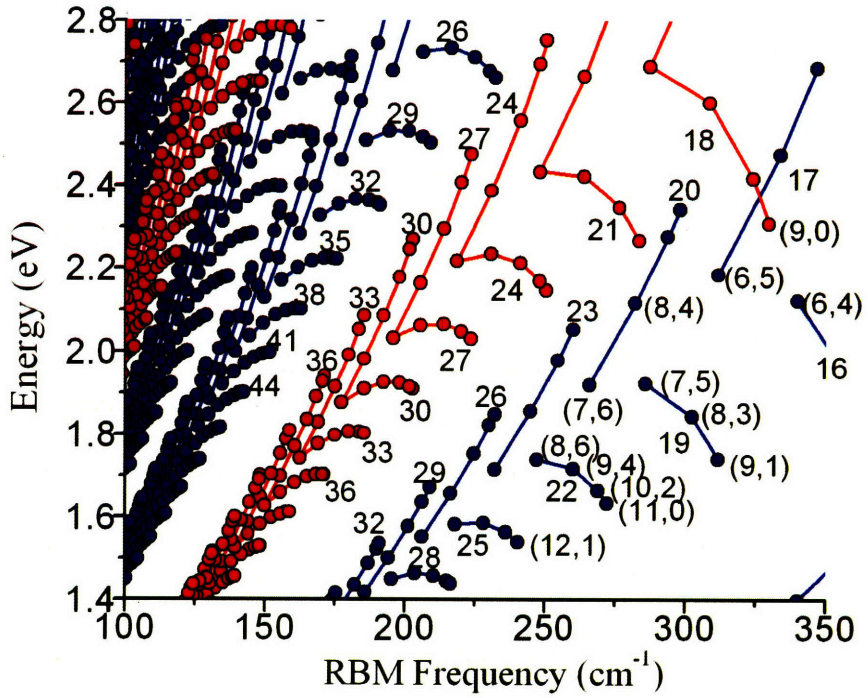

Figure 1-3: A Kataura plot based on the extended tight binding model.[7]

1.3 Scope of the Thesis

As mentioned earlier, the vibrational and electronic properties of a SWNT are largely dependent on its geometric configuration or the (n, m) number. However, there exists no commercial Raman instrument capable of efficiently collecting Raman spectrum from individual SWNTs with the large range of laser excitation energies required. The only available Raman instrument capable of tunable laser excitation ranges is

based on a triple monochomator. However, this configuration has low overall light transmission efficiency (on the order of 10%) and is not suitable for collecting Raman spectra from individual SWNTs. The first goal of this thesis work is to deign and construct a Raman instrument capable of obtaining signals efficiently from many different individual (n, m) SWNTs. Methods and tools to collect, organize and analyze a large amount of Raman spectra from many different (n, m) SWNTs using such an instrument will also be discussed.

A SWNT has a extremely large surface area to volume ratio (all the atoms of a SWNT are exposed to the environment), and these fundamental properties are sensitive to the environmental changes. Indeed, it is this sensitivity that makes a SWNT a good candidate for chemical sensors and electronic devices. Thus, to understand the fundamental properties of a SWNT and to use a SWNT in sensors and devices, it will be critical to understand the effect of the environment on the properties of a SWNT. The second goal of the work is to use resonant Raman spectroscopy to characterize individual SWNTs and to investigate how their electronic and vibrational properties change under different environmental conditions.

Due to the one dimensionality of a SWNT, the vibrational and electronic band structure of a SWNT is governed by quantum confinement effects. Thus, small changes in the physical dimensions of a SWNT are expected to strongly affect the properties of a SWNT. The third goal of the work is to investigate how various types of strain in a SWNT affect its vibrational and electronic properties.

In the next chapter, we will start with the development of a tunable Raman instrument for the study of SWNTs. Then we will focus on the study of environmental effects by studying suspended SWNTs in Chapter 3, the study of optical transition energies of metallic SWNTs by tuning laser excitation energies in Chapter 4, and the study of the effect of strain on the vibrational and electronic properties of SWNTs in Chapter 5.

Chapter 2

Raman Instrument

As mentioned in the introduction, Raman spectroscopy is a versatile tool for studying various properties of a SWNT. Specifically, the capability of a confocal Raman instrument to obtain signal from an individual SWNT has enabled various interesting research. However, in order to investigate a significant portion of the SWNTs in a typical sample, one needs a Raman spectrometer capable of multiple laser excitation energies between 1.4 eV-2.7 eV. In this chapter, we will first discuss several technical challenges when constructing such an instrument, address these challenges and provide an implementation of such a system. Finally, an overview of the finished instrument will be given.

Figure 2-1 is a simplified diagram of a typical Raman instrument, showing all essential components of a Raman instrument. When constructing a widely tunable Raman instrument, almost every component of the Raman instrument has to be tunable. Tunable laser source, tunable laser transmitting filter, tunable laser blocking filter and tunable high-efficiency spectrometer are essential for the proper operation of the instrument. In each of the following sections, exact requirements and implementation details for each of these components are discussed.

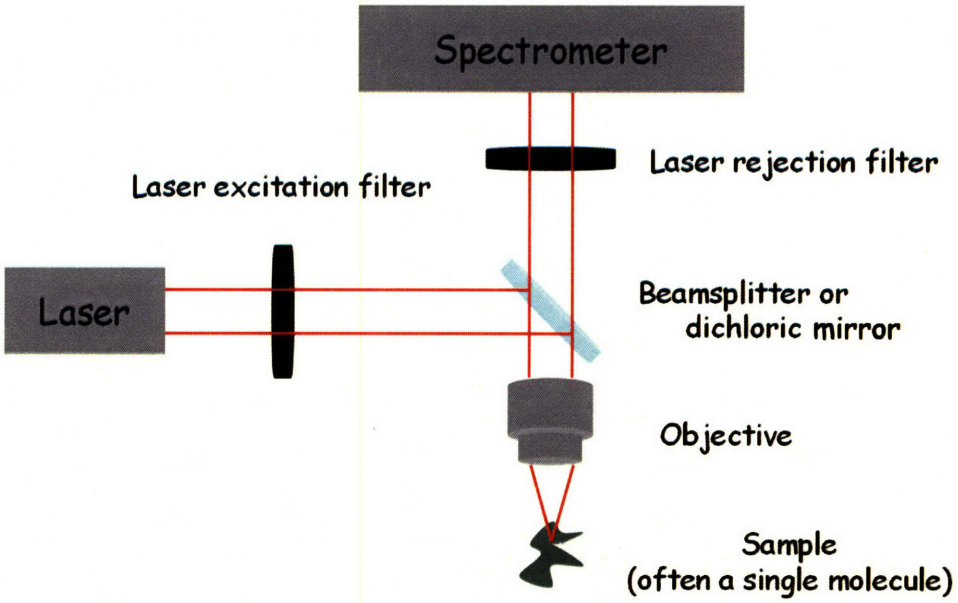

Figure 2-1: Diagram of a typical Raman instrument.

2.1 Laser Source

As mentioned earlier, laser excitation energies between 1.4 eV-2.7 eV are desirable for the study of SWNTs. At present, however, there is no single laser medium capable of continuous tuning between 1.4 eV-2.7 eV at a reasonable cost. Thus, multiple discrete line lasers and tunable lasers have to be combined to cover as much of the 1.4 eV-2.7 eV range.

An argon ion laser, a krypton ion laser, a dye laser and a titanium sapphire (Ti:Sapphire) laser were provided by the MIT spectroscopy laboratory. The argon ion laser (Coherent Innova 70C) provides laser lines at 2.71, 2.66, 2.60, 2.54, 2.50, 2.47, and 2.41 eV. The dye laser (Coherent 699), which uses Rhodamine 6G dye, covers 2.00 eV - 2.18 eV and the Ti:Sapphire laser (Coherent 899) covers 1.4 eV-1.76 eV. The krypton ion laser (Coherent 90C) lases at 1.92 eV and 1.83 eV. A recently acquired diode-pumped 10W neodymium-doped yttrium aluminium garnet (Nd:YAG) laser (Coherent Verdi V10) at 2.33 eV is used to pump the dye laser and the Ti:Sapphire laser with great pump beam pointing stability. A tunable diode laser for 1.77 eV-1.96 eV is under development.

Figure 2-2 summarizes the laser sources mentioned above. Except for a small gap between 2.18 eV and 2.41 eV, the whole 1.4 eV-2.7 eV range is covered by these laser sources with gaps smaller than 0.06 eV. Since the typical resonance window for a typical Raman process of a SWNT is ±0.03 eV to ∼ ± 0.06 eV, a SWNT with a resonance energy within any of these 0.06 eV gaps can be still observed by Raman spectroscopy.

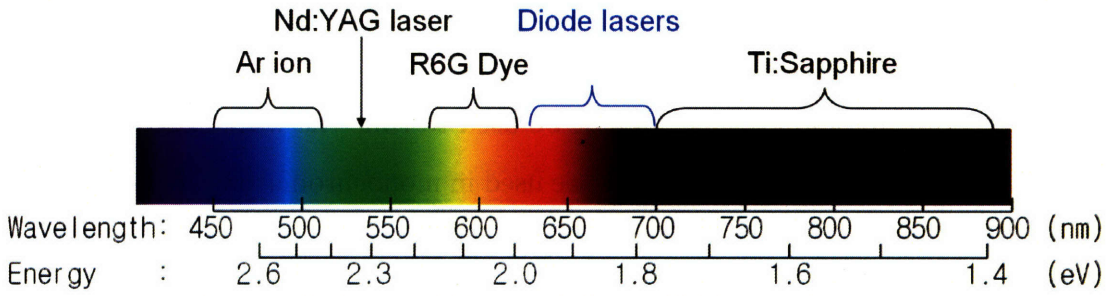

Figure 2-2: Laser tuning capabilities

2.2 Spectrometer

Most commercial Raman spectrometers are based on conventional Czerny Turner design, which utilize surface relief reflection gratings. However, there are many known problems with such gratings: high polarization dependent loss, abrupt dependence of efficiency on wavelength, and low overall diffraction efficiency (70% max for most commercial gratings).

A transmission grating based on a volume hologram, called a volume phase holographic grating (VPHG), is known to eliminate these problems. The polarization dependence can be negligible and the diffraction efficiency can be higher than 90% for many of commercially available VPHGs. The dependence of the efficiency on wavelength is typically parabolic near the efficiency maximum, which makes the spectrum obtained using these gratings smooth and easy to analyze.

To demonstrate the advantages of a VPHG mentioned above, figures 2-3 (a) and (b) show the diffraction efficiency curves of a surface relief reflection grating and a

VPHG with similar line densities and operating wavelength. The diffraction efficiency of the VPHG reaches 90% and stays well above 70% from 575 nm to beyond 900 nm, whereas the diffraction efficiency of the surface relief reflection grating is about 70% at its peak. The surface relief reflection grating shows a severe polarization dependence whereas the VPHG shows a much smaller polarization dependence. Such high diffraction efficiency over a large wavelength range and the small polarization dependence makes a VPHG an ideal component for the tunable laser filter and the tunable high-efficiency spectrometer.

However, transmission gratings cannot be used to tune the wavelength of light in the same way that the reflection gratings are used in monochromators. Thus, a unique geometry utilizing a rotating mirror and grating was devised to allow wavelength tuning using transmission gratings. Figure 2-4 shows such a geometry. The mirror and grating are rigidly fixed to each other and they can rotate around the rotational center. Using the grating equation, the following can be obtained:

$$n\lambda = d(\sin\alpha = \sin\beta) = 2d\sin\alpha. \tag{2.1}$$

Once collimators are added between the input slit and the grating, and the output slit and the mirror, we have a fully functional monochromator, whose transmission wavelength is determined by Eq. 2.1. Figure 2-5 shows a diagram of spectrometers built for this work. The collimators for the spectrometers are 1-inch diameter achromatic doublet lenses (L1 and L2) with focal length of 150 mm, resulting in an f-number of 6.6. To achieve the best transmission efficiency on the entire 1.4 eV-2.7 eV laser excitation range, two spectrometers are built. The optics for the first spectrometer is optimized for 1.8 eV - 2.7 eV whereas the optics for the second one is optimized for 1.4 eV - 1.9 eV. The gratings used for the first and the second spectrometers are 1800 lines per millimeter (lpmm) VPHG optimized at 2.33 eV and 1095 lpmm VPHG optimized at 1.77 eV, respectively.

Figure 2-6 shows the full-width half-maximum (FWHM) resolution of the spectrometers. The FWHM resolution is about $4 \sim 10$ cm^{-1} in the wavelength range

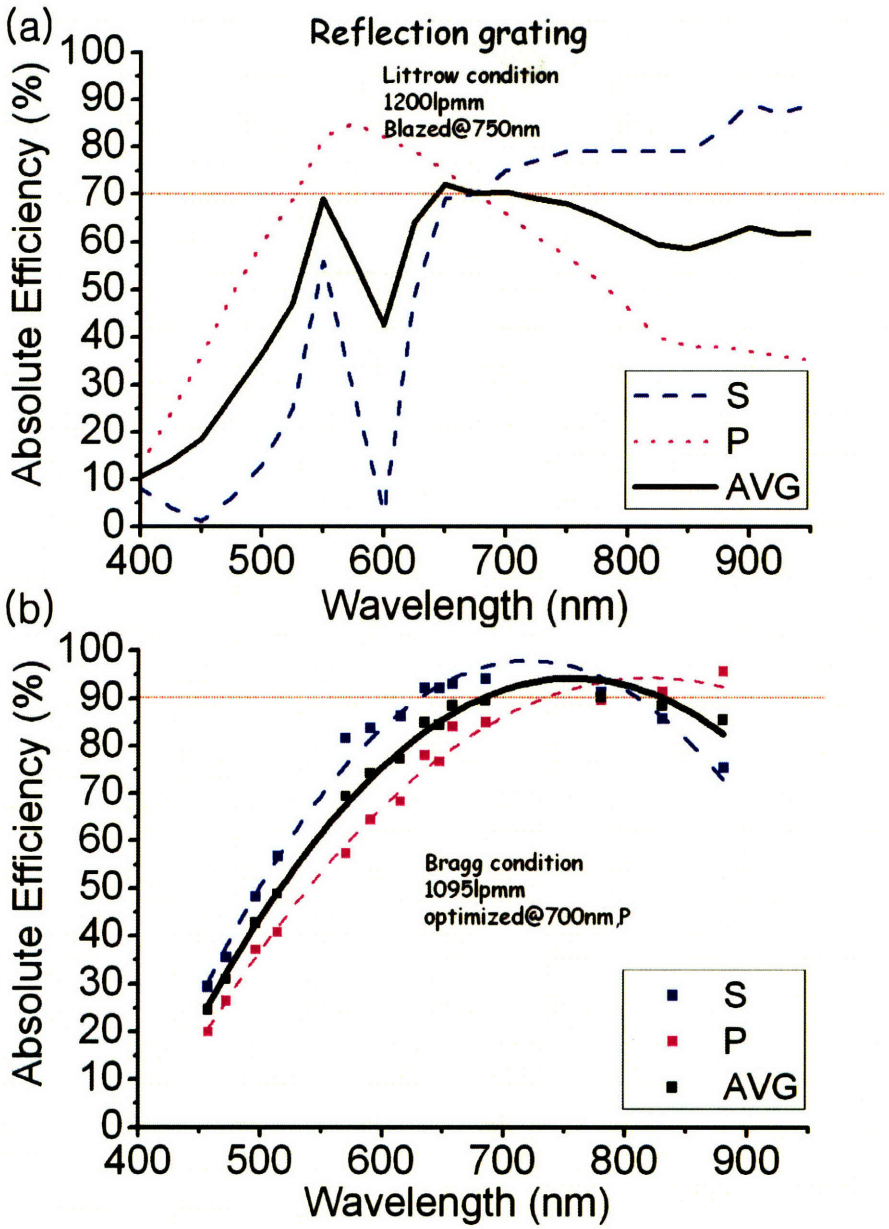

Figure 2-3: Diffraction efficiency curves of (a) a surface relief grating at the Littrow condition and (b) a VPHG at the Bragg condition. The data for the reflection grating was obtained from Optometrics Corporation. The data for VPHG was measured with a VPHG purchased from Wasatch Photonics.

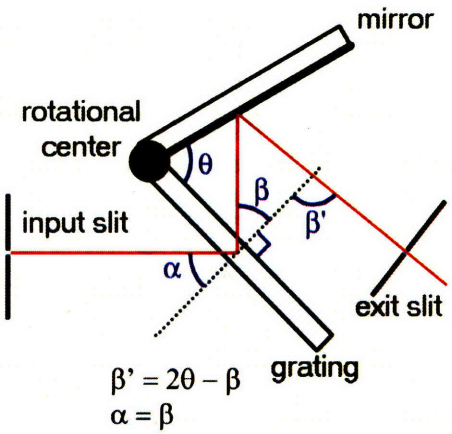

Figure 2-4: A basic monochromator design based on a transmission grating assembly.

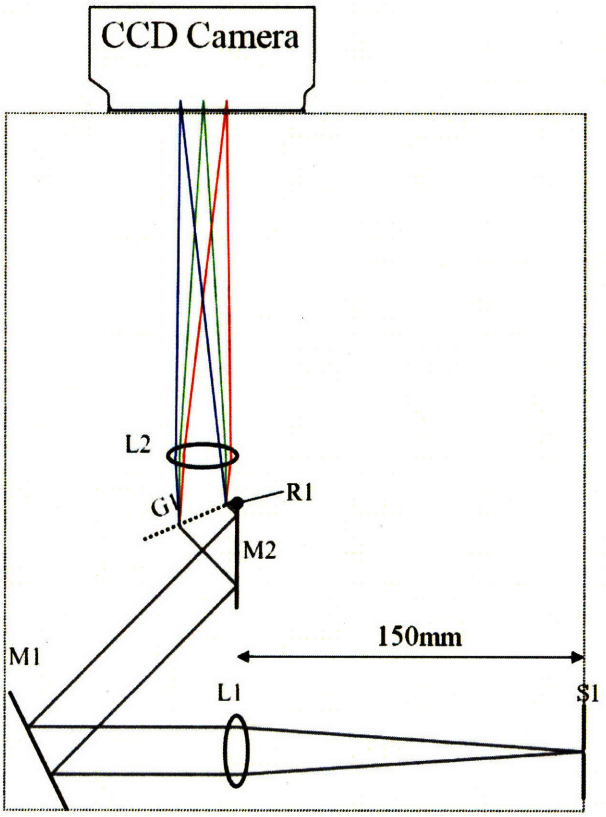

Figure 2-5: A schematic diagram of the spectrometer. S1 is the entrance slit. L1 and L2 are achromatic doublet lenses with focal length of 150mm. M1 and M2 are silver mirrors. G1 is the VPHG and rotates with M2 around the rotational center R1.

where the spectrometers are optimized. Since there a tradeoff between the FWHM resolution and the bandwidth, we cannot push the resolution arbitrarily high. The ratio of the bandwidth to the FWHM resolution is equal to the ratio of CCD detector size ($\simeq$ 26 mm) to the focused beam spot size on the CCD detector ($\simeq$ 60 μm), which is about 440. We need a minimum bandwidth of 1600 cm^{-1} to capture most important Raman features of a SWNT in one accumulation, the minimum value of the FWHM resolution shall be greater than 4 cm^{-1}.

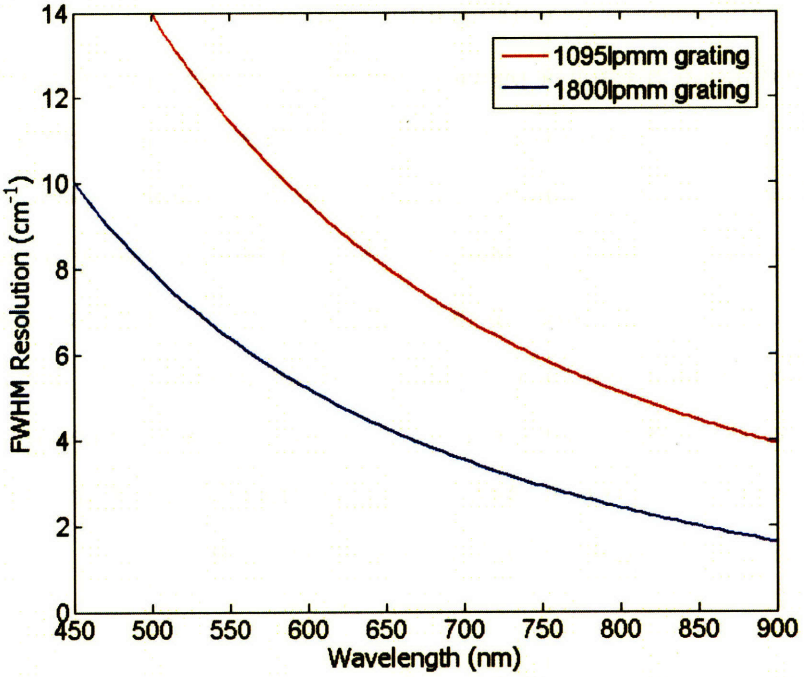

Figure 2-6: The full-width half-maximum resolution of the spectrometers as a function of wavelength. The red line and the blue line are the resolution with 1095 lpmm grating and 1800 lpmm grating, respectively.

2.3 Laser Transmitting Filter

A typical laser source has significant spectral noise, such as amplified spontaneous emission or plasma lines. Such noise is harmful for sensitive spectroscopy techniques such as Raman spectroscopy or photoluminescence spectroscopy. Thus, the spectral

noise is filtered by a laser transmitting filter or a laser line filter before the laser reaches the sample.

There are several ways to filter out the spectral noise. In a fixed laser wavelength Raman instrument, thin-film interference bandpass filters with bandwidth of 1 - 10 nm are the best choice due to their high transmission efficiency, reliability, low cost and simplicity. However, the center wavelengths of these filters are fixed when the filters are manufactured, making their usage in a tunable Raman instrument limited. Thus, in a widely tunable Raman instrument, a prism or grating based monochromator is required as a tunable laser transmitting filter element.

A prism based monochromator provides higher transmission efficiency than a grating based monochromator. However, a prism based monochromator has lower spectral resolution than a grating based monochromator due to the low dispersion of a prism and provides insufficient noise rejection for a Ti:Sapphire laser or a dye laser.

Figure 2-7 is a schematic diagram of the laser transmitting filter constructed for this work. The layout is similar to the spectrometer mentioned in the previous section. The difference is that, since the incoming light is already collimated, there is no collimator needed for the incoming beam in a laser transmitting filter. Instead, there is a spatial filter assembly (L1 and L2) for the outgoing beam.

2.4 Laser Blocking Filter

The role of the laser blocking filter is to block off only the laser light reflected from the sample so that relatively weak Raman signal can be detected without saturating the detector with stray laser light. Typically, the filter is required to block off 99.9999% of the laser light (equivalent to an optical density of 6 (OD6)) without degrading the Raman signal. Since one of the most important Raman features, the RBM, typically has a frequency shift between 100 cm^{-1} and 300 cm^{-1}, the laser filter must have a sharp transition width equal to or less than 100 cm^{-1} between OD6 and OD0.3.

Furthermore, the transition wavelength of the filter must be tunable to match the wavelength range of the available laser source. Holographic long wave pass edge

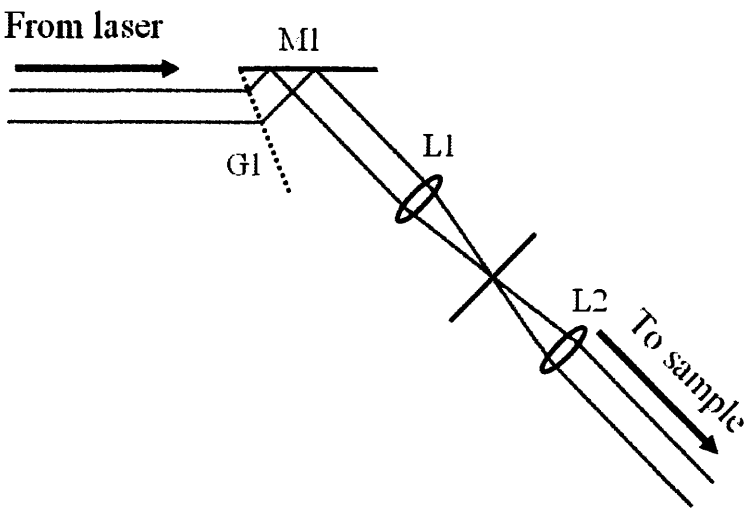

Figure 2-7: A schematic diagram of a laser transmitting filter. L1 and L2 are achromatic doublets with a focal length of 50mm. G1 is an 1095 lpmm VPHG optimized at 700nm. M1 is a silvered mirror. The diameter of the pinhole between L1 and L2 is 25 μm.

filters from Semrock could meet all of these requirements, if properly used. They are advertised to have a sharp transition width (0.5% of laser wavelength) and OD6 at the laser wavelength. Their transition wavelength is blue-shifted up to 11% of its specified wavelength when the filter is rotated by 45 degrees from the normal to the incident beam. For example, filter specified at 785 nm can be used for laser excitations from 700 nm to 785 nm. However, the amount of blue shift is different for p-polarization and s-polarization. Since the shift for p-polarization is greater, a p-polarizer is placed before the filter to maximize the tuning range.

Since each filter is tunable up to 11%, a set of six filters will fulfill the tunability requirements between 1.4 eV-2.7 eV.

2.5 The Instrument

Figure 2-8 shows how individual components are assembled into a Raman instrument. Since there are multiple laser sources, there are also multiple laser beams that are spatially separated. A laser selector unit, which is a silver mirror mounted on a rotational platform, directs one necessary laser beam into the tunable laser filter at a

time. About one third of the filtered laser beam is reflected by the beamsplitter and enters the microscope. This beam reaches the sample on the microscope through an objective and the scattered light is collected with the same objective. The collected light travels back on the same path as the incoming laser beam and passes through the laser blocking filter before it reaches one of the spectrographs.

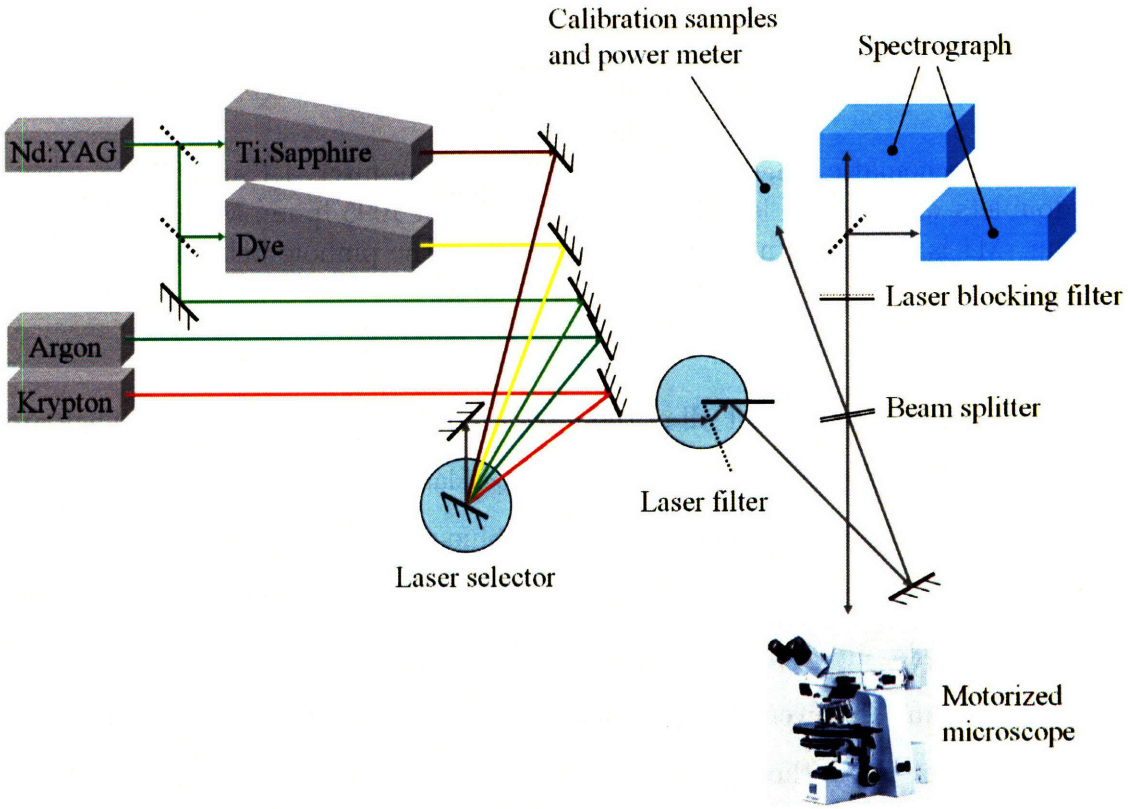

Figure 2-8: A schematic diagram of the Raman instrument.

2.6 Electronic Control

Most components of the Raman instrument that require precise motion or frequent adjustments are motorized and controlled by a single software package running on a control computer. The motorized components include the laser selector, laser transmitting filter, calibration sample holder containing multiple samples, spectrographs,

and the microscope stage.

The laser selector and laser transmitting filter are mounted on worm-gear driven motorized rotational stages actuated by stepper motors (Micro Motion Technology AR-600-2S). The control software stores the precise angular coordinate of the laser selector corresponding to each laser, allowing the user to change from one laser to another within seconds. The wavelength of the laser transmitting filter can also be set using the control software, with a wavelength resolution of 0.1 nm.

The calibration sample holder holds multiple wavenumber calibration samples and a laser power meter. The wavenumber calibration samples in use are naphthalene, sulfur, and acetonitrile. With the control software, the user can select one of the calibration samples or the laser power meter. The advantage of this configuration is that, since the calibration samples are mounted outside the microscope, the wavenumber calibration can be performed without removing the user's sample on the microscope stage, allowing a quick change of the laser excitation wavelength. The standard calibration procedure using the aforementioned calibration sample holder is programmed in the control software and typically takes less than a couple of minutes to complete.

Chapter 3

Suspended Single Wall Carbon Nanotubes

3.1 Introduction

Isolated suspended SWNTs, by virtue of their unperturbed environment, have provided unique opportunities for furthering our understanding of SWNT properties, such as greatly enhanced transport signals [8] and strong band-gap photoluminescence [2]. In this chapter, we show that the suspended SWNTs also offer unique opportunities for Raman scattering studies, including enhanced Raman signals, decreased linewidths of the radial breathing modes (RBMs) and the observation of intermediate frequency modes (IFMs) at the single nanotube level.

During the past few years, the effects of the environment (such as the wrapping of SWNTs with sodium dodecyl sulfate (SDS) [9] and DNA [10]) and of the substrate on the optical properties of SWNTs (such as photoluminescence (PL) [9, 10, 2] and Resonance Raman Spectroscopy results [10, 11, 12, 13]) have been studied in some detail. The optical spectra give information on both the electronic transition energies E_{ii} and the phonon band structure and their dependence on the environment. For example, the PL spectra taken from both SDS-wrapped SWNTs and suspended SWNTs show that the E_{ii} of SDS-wrapped SWNTs are shifted when compared to suspended SWNTs, while the RBM frequencies ω_{RBM} are less affected [14]. However,

previously reported works are limited to ensembles of SWNTs.

This chapter presents a Raman spectroscopy study both of individual suspended SWNTs, which minimize environmental effects, and of individual SWNTs on a heavily n-doped polycrystalline silicon (poly-Si) substrate. Both of these environments, as is shown below, offer special research opportunities. The work presented in the following sections is also published in Ref. [15].

3.2 Experiment

The suspended SWNTs are grown across two poly-Si electrodes, which serve both as electrical contacts and as elevated structures for suspending the SWNTs. The poly-Si electrodes are fabricated using standard silicon technology (see Fig. 3-1). Firstly, a 1μm-thick poly-Si film is grown by chemical vapor deposition (CVD) on top of a silicon substrate with a 1μm-thick thermally grown SiO_2 film (see Fig. 3-1(a)). Then, photolithography and a reactive ion etch are used to pattern the poly-Si film and the oxide film (see Fig. 3-1(b)).

The electrodes have two regions: the narrow trench region (1$\sim$4μm wide) and the wide trench region (10μm wide) (see Fig. 3-1 (d)). During the SWNT growth, a high electric field on the order of 10^6V/m can be selectively applied across the narrow trenches only. A high electric field is known to enhance the growth rate of SWNTs and to align them [16, 17]. Moreover, by controlling the maximum length of the SWNTs, one can guarantee that there are no suspended SWNTs growing across the wide trench, as shown in Fig. 3-2(b).

The SWNTs are grown directly on the sample by a methane CVD process [18]. Samples were prepared both with and without applied electric fields between the electrodes (see Fig. 3-2). The iron catalyst nanoparticles are prepared by mixing 50.5mg of iron(III) nitrate, 21mg of sodium hydrogen carbonate, and 50mL of deionized water and stirring the mixture for 1$\sim$4hrs [19]. To deposit the catalyst particles, the samples are dipped in the catalyst suspension for 1 and 5 minutes to produce low-density (LD) and high-density (HD) samples, respectively (see Fig. 3-2). Then, the samples are washed with ethanol and blown dry with nitrogen at room temperature. Finally, the SWNTs were grown at 800$\sim$900°C in the flow of methane (100 sccm), hydrogen (50 sccm), and argon (100 sccm) in a 1-inch tube furnace.

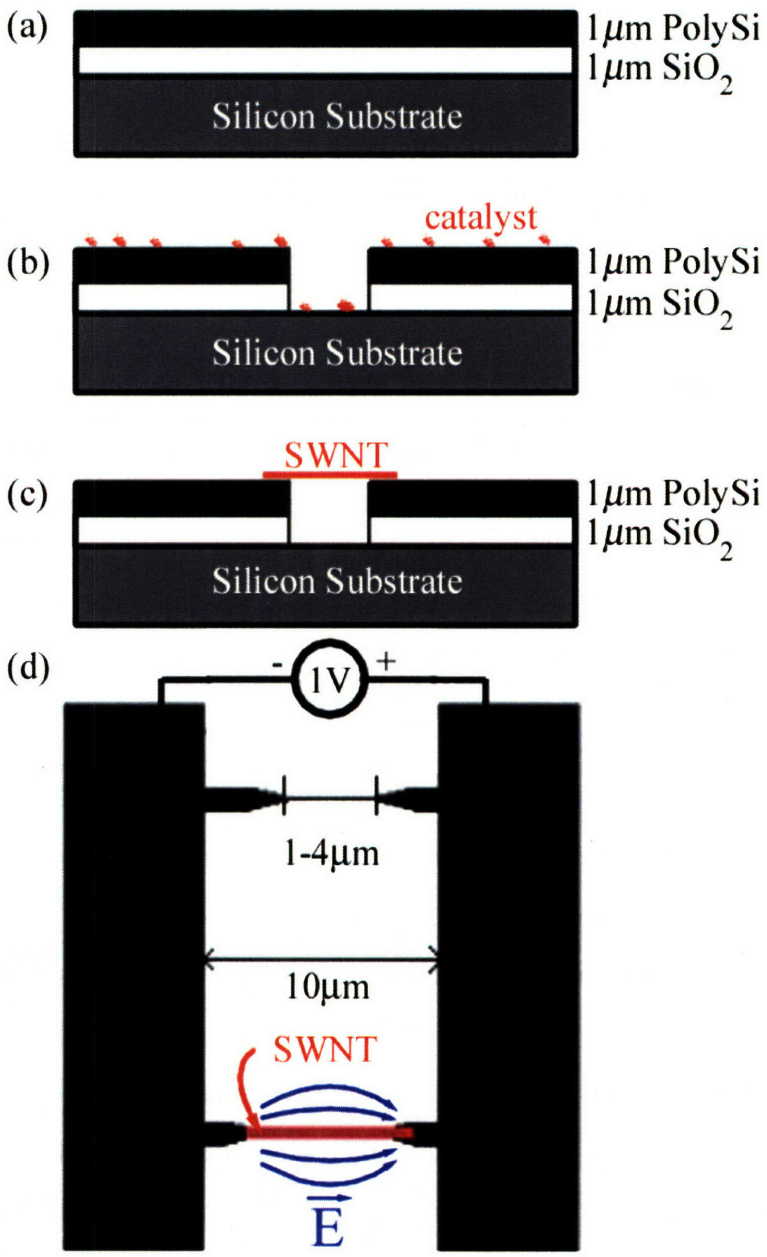

Figure 3-1: The electrode structure and SWNTs grown on the electrodes. (a) and (b) are the side view of the electrode structure before and after patterning, respectively. (c) shows the electrode structure and a suspended SWNT grown on the electrode. (d) is the top view of the electrode structure after patterning.

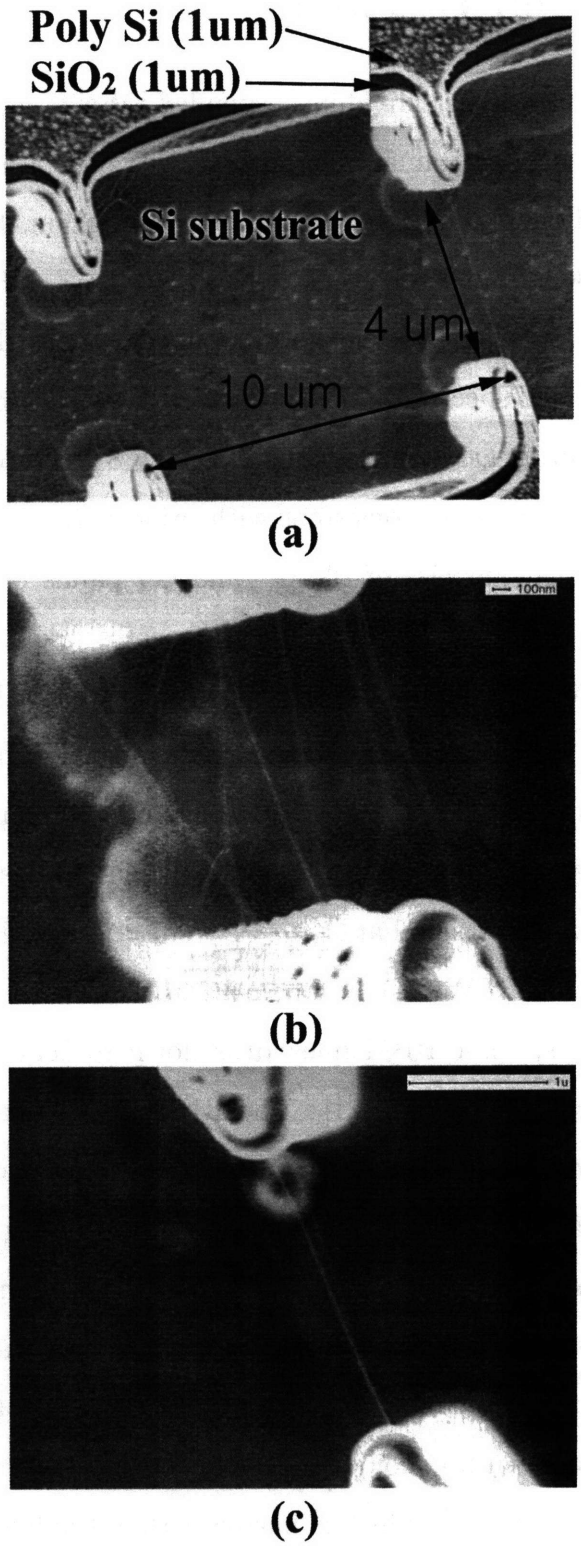

Figure 3-2: SEM images of (a) the electrode structure, (b) HD suspended SWNTs grown without an applied electric field, and (c) LD suspended SWNTs grown with an applied electric field. The magnification is the same for (b) and (c).

3.3 Results and Discussion

Raman spectra were taken from individual suspended SWNTs and individual SWNTs on a poly-Si substrate using a Raman microprobe laser system in the back-scattering geometry and E_{laser}=1.58eV and 2.41eV laser energy excitation. Figure 3-3(a) presents a Raman spectrum taken from a single suspended SWNT using E_{laser}=1.58eV, where a strong RBM signal, as well as intermediate frequency modes (IFMs) and relatively narrow G^+ and G^- band spectra (FWHM linewidth=8cm^{-1} for both G^+ and G^- bands) are observed. From ω_{RBM}, the diameter of the SWNTs can be derived. The G^- and G^+ mode frequencies are consistent with prior work on the relation between the A-symmetry mode frequencies of the G^- and G^+ bands based on their diameter. [20]. Figures 3-3(b) and 3-3(c) show Raman spectra taken from one suspended SWNT and another SWNT on a poly-Si substrate, respectively. For both spectra, we have ω_{RBM} =237cm^{-1} and both spectra show a particularly low intensity for the anti-Stokes RBM band compared to the Stokes RBM band. Raman signals taken from both SWNTs are enhanced compared to the Raman signal taken from SWNTs on a Si/SiO_2 substrate for which a signal at ω_{RBM} =237cm^{-1} is also shown in Fig. 3-4.[11] Full width half maximum (FWHM) RBM linewidths down to 3cm^{-1} are observed from suspended SWNTs, while RBM linewidths down to 5cm^{-1} are observed from the SWNTs on a Si/SiO_2 substrate [21]. The RBM bands taken from SWNTs on a poly-Si substrate are usually stronger than the RBM bands taken from suspended SWNTs and often feature the second harmonic, as shown in Fig. 3-3(c) at 475cm^{-1}. These enhanced intensities might be attributed to a surface enhanced Raman effect from a rough poly-Si surface, where the polycrystalline grain size is about several tens of nanometers. Similar enhanced signals have been reported for SWNTs on rough metal surfaces and on a colloidal silver cluster substrate [22]. The linewidth of the second harmonic is 8cm^{-1}, which is narrower than the linewidth of the second harmonic of RBM bands reported for SWNT bundles [23].

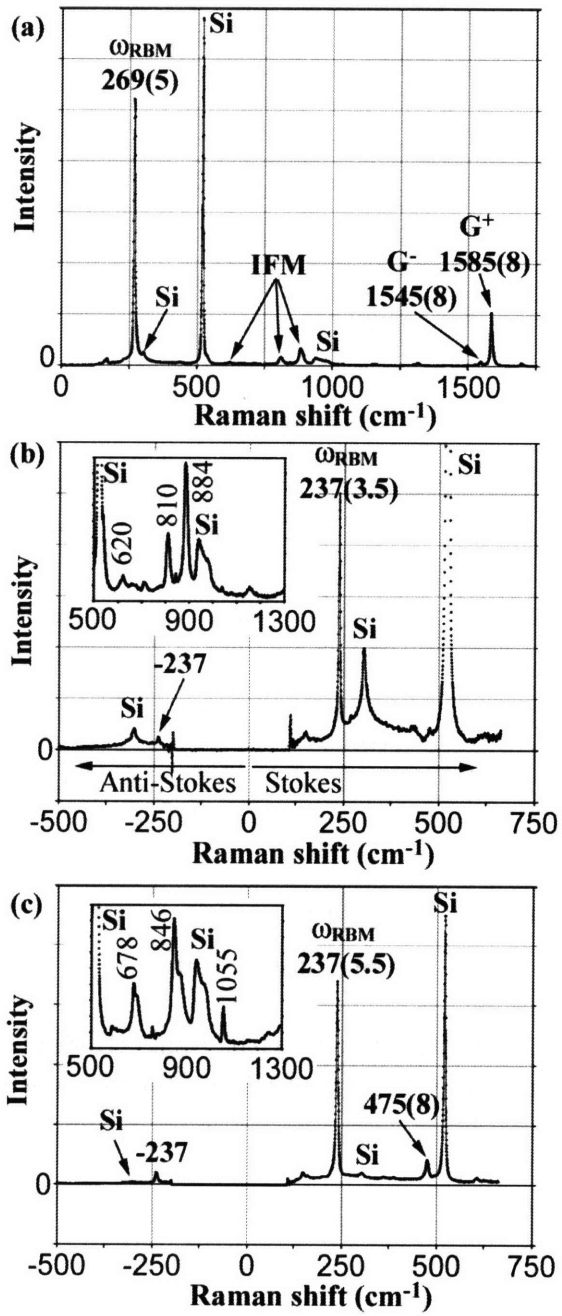

Figure 3-3: The Raman spectra taken with E_{laser}=1.58eV from: (a) and (b) individual suspended SWNTs, and (c) an individual SWNT on a poly-Si substrate. The RBM band and G^- band frequencies (FWHM linewidths) are shown. The insets in (b) and (c) are, respectively, the IFMs taken from an individual suspended SWNT and an individual SWNT on a poly-Si substrate, different from the SWNTs for which the RBM spectra are shown.

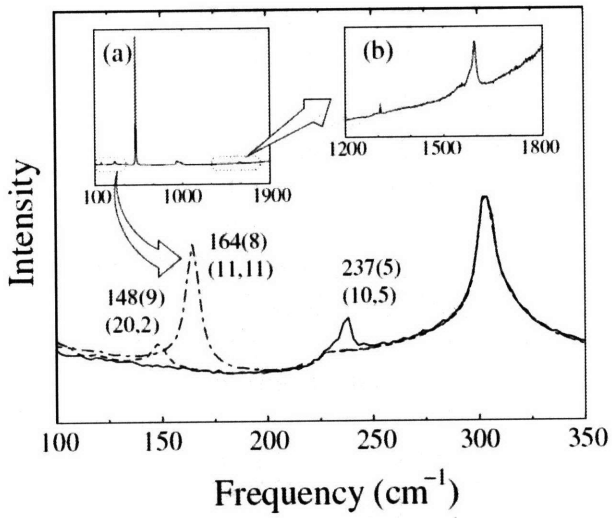

Figure 3-4: The Raman spectra taken with E_{laser}=1.58eV from three individual SWNTs on a Si/SiO_2 substrate.[11] The peak at 303cm^{-1} corresponds to a Si peak.

3.4 The Intermediate Frequency Modes

The inset figures of Figs. 3-3(b) and 3-3(c) show the rich IFM spectra taken from a suspended SWNT and a SWNT on a poly-Si substrate, respectively. IFM spectra were previously observed only in SWNT bundles [24, 25]. Due to the enhanced signal, detailed structure in the IFM region can be seen. The IFMs are related to the phonon band structure and might give information on the chirality of individual SWNTs [25]. Some similar modes have been observed in the IR spectra taken from SWNTs [26].

To compare the IFM spectra obtained from individual SWNTs to IFM spectra obtained from SWNT bundles, the IFM spectra reported in Ref. [25] are reproduced in Fig. 3-5. Six representative IFM spectra obtained from individual SWNTs are shown in Fig. 3-6. Since the laser excitation energies used in Ref. [25] and in this chapter are different, a direct comparison cannot be made.

In Fig. 3-5(a), there are three modes whose frequencies are not dependent on the E_{laser}. These three modes appear at 650~700 cm^{-1}, 850~870 cm^{-1}, and 1050~1090 cm^{-1}. All of these modes also show up in individual SWNT spectra but the relative intensities among different modes vary greatly from one SWNT to another. Sometimes, there are IFM modes found at 600~650 cm^{-1} from individual SWNTs. The origin of these modes are currently unknown.

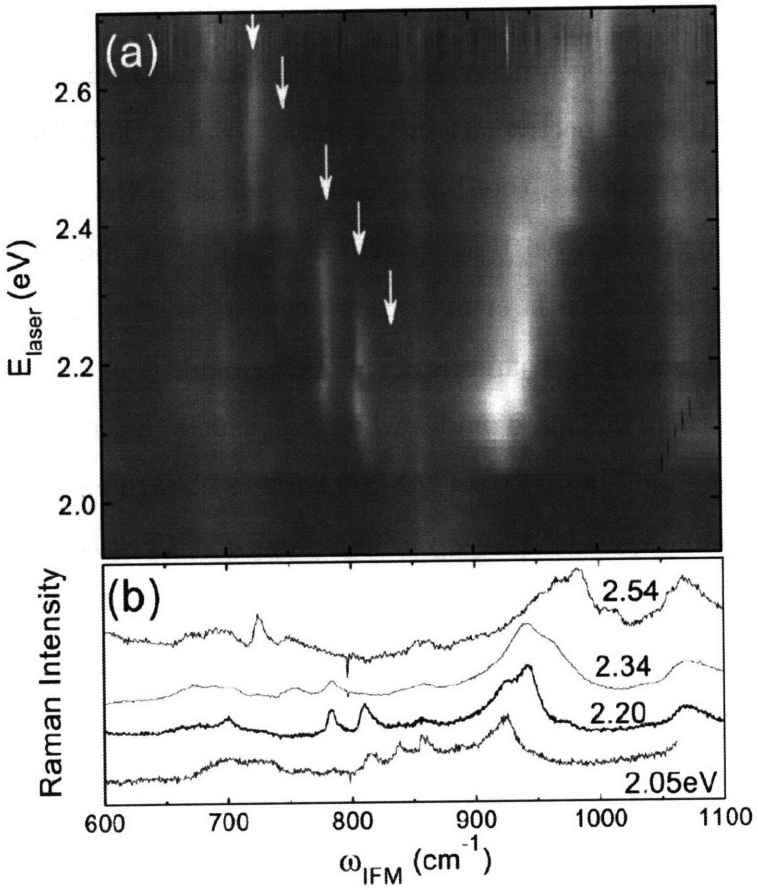

Figure 3-5: (a) Two-dimensional plot for the E_{laser} dependence of the Raman spectra of SWNT bundles in the IFM range. The light areas indicate high intensity. (b) Raman spectra in the IFM range taken with E_{laser} 2.05, 2.20, 2.34, and 2.54 eV.

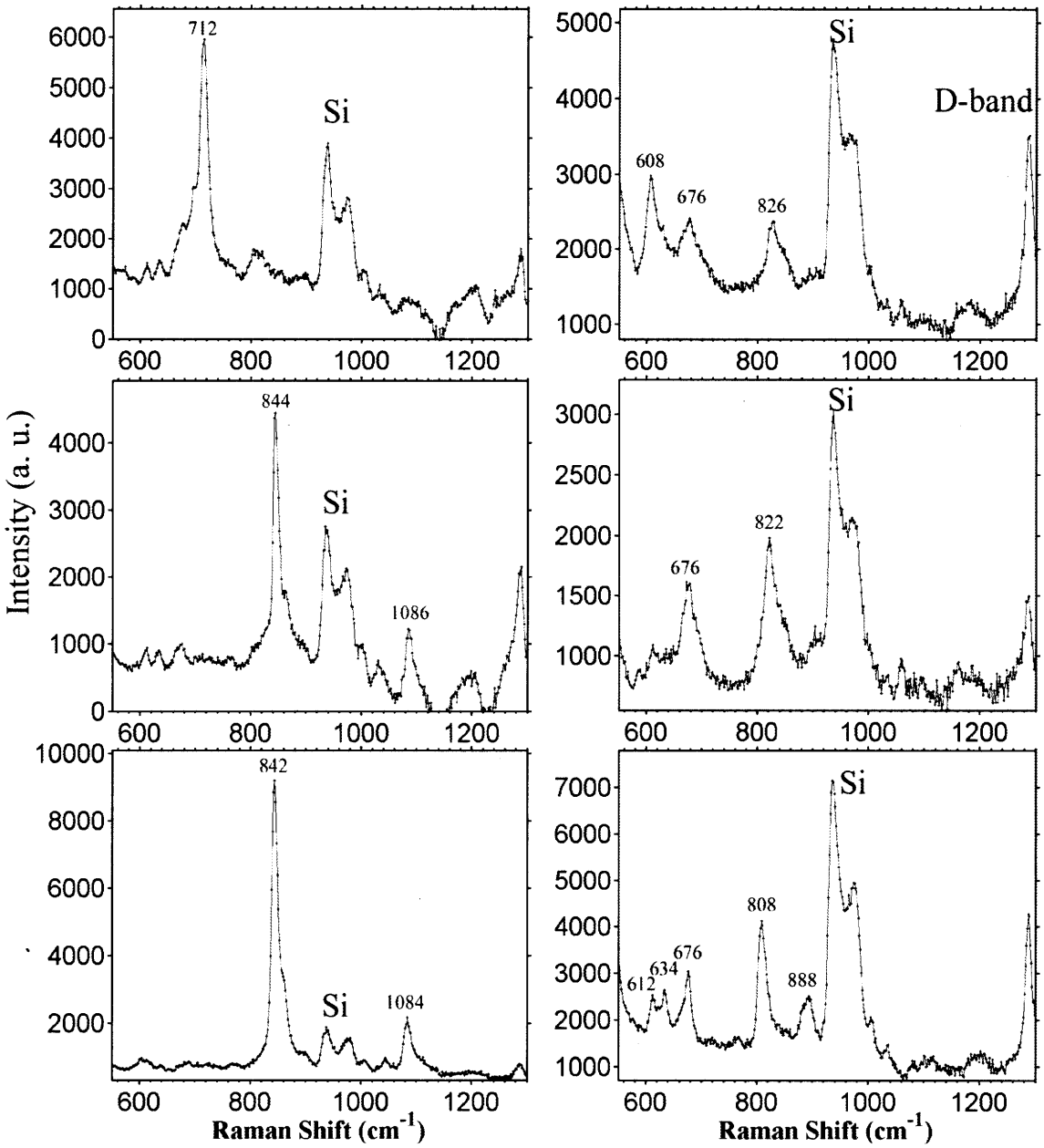

Figure 3-6: (a) Six representative IFM spectra obtained from individual SWNTs. The common peak at 900∼1000 cm^{-1} is a Si peak. Another common peak at about 1300 cm^{-1} is a D-band.

3.5 Conclusion

Enhanced signals from suspended SWNTs allow a study of normally weak modes, such as IFMs, at the single nanotube level. Such enhanced signals also have been shown to enable in-situ monitoring of SWNT growth.[27]

Narrow linewidths indicate a relatively unperturbed environment, which leaves room for studying the effects of selected perturbations. Such an unperturbed environment is shown to contribute to possible hot phonon generation in suspended SWNTs in transport experiments and is related to the observed negative differential conductance in suspended SWNTs.[28]

Chapter 4

Metallic Single Wall Carbon Nanotubes

4.1 Introduction

Except for armchair nanotubes, two different optical transitions for metallic SWNTs are expected due to the trigonal warping effect, one with a lower transition energy E_{11L}^{M} and a second with a higher transition energy E_{11H}^{M}.[6] Although many experimental data are available for E_{11L}^{M} from previous Raman studies [14, 29], transitions associated with E_{11H}^{M} were not observed in these Raman studies, and this has remained an open question. A recent work has reported E_{11H}^{M} transitions using Rayleigh scattering and has attributed the lack of the observations of E_{11H}^{M} transitions in previous Raman experiments to the different electron-phonon coupling strengths for E_{11L}^{M} and E_{11H}^{M} transitions.[3] However, no experimental evidence is given for the difference in electron-phonon coupling strengths for E_{11L}^{M} and E_{11H}^{M} transitions.

In this chapter, we will focus on the observation of E_{11H}^{M} optical transitions for metallic nanotubes and show that the Raman signal intensity variations for the radial breathing mode (RBM) between different optical transitions provide a good match with the predictions of the ETB model, which includes excitonic effects and different coupling strengths for E_{11L}^{M} and E_{11H}^{M} transitions. The slight downshifts of the experimental transition energies for some observations are explained in terms of en-

vironmental effects.[30, 31] The work presented in this chapter is published in Ref. [32].

Figure 4-1 is a zoomed-in version of the "Kataura Plot" shown in Chapter 1.[7] Due to the trigonal warping effect, the family lines are split into two branches for each $2n+m$ metallic SWNT family.[6, 7] The lower and higher energy branches correspond to the $E^{\mathrm{M}}_{11\mathrm{L}}$ and $E^{\mathrm{M}}_{11\mathrm{H}}$ transitions, respectively.[7]

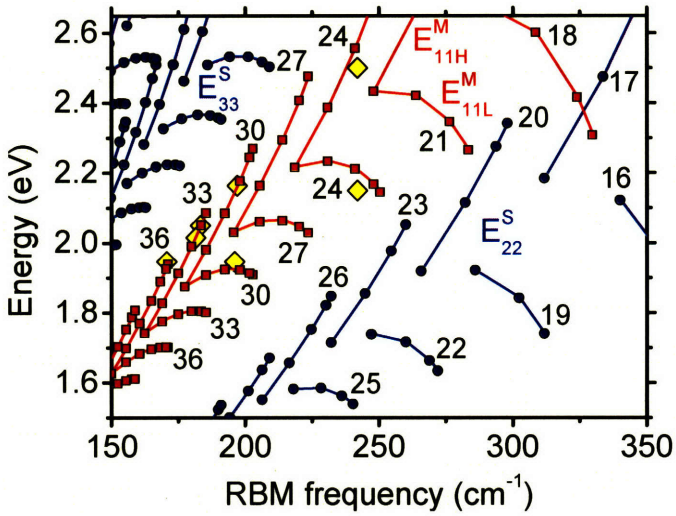

Figure 4-1: ETB+MB calculations of the optical transition energies versus ω_{RBM}. The blue circles and the red squares denote semiconducting and metallic SWNTs, respectively. The $2n + m = constant$ families are denoted by solid lines and the $2n + m$ family numbers are also indicated. The yellow diamonds are experimental $E^{\mathrm{M}}_{11\mathrm{H}}$ and $E^{\mathrm{M}}_{11\mathrm{L}}$ optical transition energies.

4.2 Experimental

Individual SWNTs are grown on a SiO_2 substrate by chemical vapor deposition (CVD) in methane at 900°C using iron nanoparticles as the catalyst.[33] The as-grown SWNTs are analyzed with a confocal micro-Raman setup with a 50× objective (NA = 0.8). The laser spot size is about $1\mu\mathrm{m}^2$. Raman spectra are taken at 16 different laser excitation energies E_{laser} from 1.56eV to 2.61eV generated from an Argon ion laser and a dye laser (R6G and DCM dye). At most of these 16 E_{laser} values, Raman spectra were taken over a 40μm by 20μm spatial area at a 0.5μm by 1μm spacing,

resulting in 1701 spectra at each laser energy. A unique shaped feature on the sample is used as a marker to identify the same spatial area at every laser excitation energies. As a result, about 150 SWNTs with diameters smaller than 1.5nm were found in this spatial region, which ensures that the density of SWNTs is low enough, so that each Raman spectrum is essentially the spectrum of an individual SWNT or only a few SWNTs at most. This spatial mapping method allows us to follow and identify each nanotube, regarding its spatial position, and the method is particularly useful for recognizing when a particular SWNT goes in and out of resonance and for obtaining a resonance profile of each SWNT as a function of E_{laser}.[34, 35] Since the repeatability of the microscope stage is better than 0.5μm, the resolution of the spatial mapping (0.5μm by 1μm) determines the accuracy of locating the spatial position of the nanotube. The RBM signals from the SWNTs are recorded simultaneously with the Raman signal from the Si, which is used for calibration. When the RBM signals at the same frequency appear at the same location at two different E_{laser} values, it can be claimed that the signals are coming from the same physical SWNT.[34] Figures 4-2(a) and 4-2(b) show such RBM signals at the same frequency (240cm^{-1}) at the same location at two different E_{laser} (2.54eV and 2.16eV, respectively).

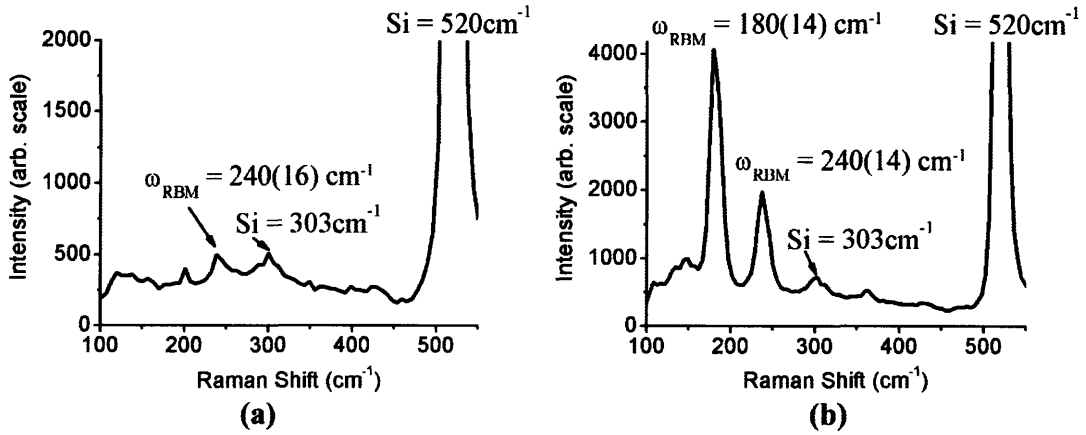

Figure 4-2: RBM signals at the same spatial position at two different laser excitation energies (a) 2.54eV and (b) 2.16eV. The ω_{RBM}=240cm^{-1} feature appears in both spectra. The numbers in parentheses are the FWHM linewidths.

4.3 Results and Discussion

By varying E_{laser} and compiling the RBM intensities obtained at each different E_{laser}, an interesting two-peak resonance window for this SWNT can be obtained (see Fig. 4-3(a)). Since no semiconducting SWNTs with ω_{RBM}=240cm^{-1} are resonant at any of the laser energies used, this is a metallic SWNT (see Fig. 4-1). The red circles represent the experimental integrated RBM intensity of this SWNT. The black curve shows the calculated resonance profiles for the integrated RBM intensity for both $E_{11\text{L}}^{\text{M}}$ and $E_{11\text{H}}^{\text{M}}$ transitions obtained from time-dependent third-order perturbation theory:

$$I(E_{\text{l}}) = C \left| \frac{m_{1\text{L}} M_{1\text{L}}^{\text{se}} M_{1\text{L}}^{\text{ep}} M_{1\text{L}}^{\text{la}}}{(E_{\text{l}} - E_{11\text{L}}^{\text{M}} - i\Gamma)(E_{\text{l}} - E_{\text{ph}} - E_{11\text{L}}^{\text{M}} - i\Gamma)} + \frac{m_{1\text{H}} M_{1\text{H}}^{\text{se}} M_{1\text{H}}^{\text{ep}} M_{1\text{H}}^{\text{la}}}{(E_{\text{l}} - E_{11\text{H}}^{\text{M}} - i\Gamma)(E_{\text{l}} - E_{\text{ph}} - E_{11\text{H}}^{\text{M}} - i\Gamma)} \right|^2, \tag{4.1}$$

where E_{l} is the laser excitation energy, $M_{1\text{X}}^{\text{se}}$,$M_{1\text{X}}^{\text{ep}}$, and $M_{1\text{X}}^{\text{la}}$ $(X = L, H)$ are the transition matrix elements for the spontaneous emission, electron-phonon scattering, and light absorption processes, respectively, E_{ph} is the RBM phonon energy, Γ is the broadening factor, and C includes all the other factors.[36] The effective masses $m_{1\text{L}}$ and $m_{1\text{H}}$ arise from the integration of the electron joint density of states, assuming that the transition matrix elements are independent of the wavevector in the range of reciprocal space contributing to the Raman intensity.[36] It should be noted here that optically excited states in SWNTs are excitonic in nature.[37, 38] However, Eq. (4.1) is restricted to non-interacting excitations, since the exciton-photon and exciton-phonon transition matrix elements only for $E_{11\text{L}}^{\text{M}}$ are available in the literature.[39] The interference between the $E_{11\text{L}}^{\text{M}}$ and $E_{11\text{H}}^{\text{M}}$ transitions is not considered since $E_{11\text{H}}^{\text{M}}$-$E_{11\text{L}}^{\text{M}}$ is large compared to Γ and E_{ph} for the SWNTs investigated.

From the optical transition energy of the highest intensity RBM peak and its RBM frequency, the SWNT in Figs. 4-2 and 4-3(a) is determined to be a (10,4) SWNT (see Fig. 4-1). ETB calculations for the (10,4) SWNT give the effective mass ratio $m_{1\text{L}}/m_{1\text{H}} = 0.46$[40] and the matrix element ratios $M_{1\text{L}}^{\text{la}}/M_{1\text{H}}^{\text{la}} = M_{1\text{L}}^{\text{se}}/M_{1\text{H}}^{\text{se}} = 1.25$[41], and $M_{1\text{L}}^{\text{ep}}/M_{1\text{H}}^{\text{ep}} = 3.75$[42]). A ratio of 7.26 between the integrated intensities of the

E_{11L}^{M} and E_{11H}^{M} peaks is found, as shown by the blue diamonds in Fig. 4-3(a). In order to fit the black curve from the above equation with our experimental data points, one needs to adjust the broadening factor Γ and to make an overall downshift of both E_{11L}^{M} and E_{11H}^{M}. Both the energy splitting between E_{11L}^{M} and E_{11H}^{M} (0.35eV) and their integrated intensity ratio agree well between theory and experiment. There is, however, a downshift of 72meV between the experimental results for both E_{11L}^{M} and E_{11H}^{M} when compared to the theoretical predictions. Since both E_{11L}^{M} and E_{11H}^{M} downshift by the same amount, the energy downshift is likely to be due to the different dielectric environment for our SWNTs as compared to SDS-wrapped SWNTs.[30, 31] The presence of other SWNTs can cause an inhomogeneous dielectric environment even on the same substrate. The curve fitting gives rise to Γ=35meV for all the three SWNTs shown in Fig. 4-3, which is also comparable to Γ values obtained in previous experiments.[43, 44, 45] The close match in the RBM intensity between the matrix element calculation and the experimental result indicates that the different intensities of the two resonances are due to differences in the matrix elements. Note that the ratio in the total optical matrix elements including the effective mass correction ($m_{1L}M_{1L}^{la}M_{1L}^{se}/m_{1H}M_{1H}^{la}M_{1H}^{se} = 0.72$) is much closer to one than the ratio in the electron-phonon coupling matrix elements ($M_{1L}^{ep}/M_{1H}^{ep} = 3.75$). Thus, the electron-phonon coupling matrix elements dominate the difference in the intensities for this particular case.

Table 4.1 lists data for two other metallic SWNTs in addition to three metallic SWNTs shown in Fig. 4-3, for which the E_{11H}^{M} resonance was observed. For the $(10, 4)$ and $(13, 4)$ nanotubes, the resonant Raman signal at both the E_{11L}^{M} and E_{11H}^{M} energies are detected, whereas, for the rest of the nanotubes, the E_{11L}^{M} resonance was not detected due to the lack of a laser excitation source. However, their E_{11H}^{M} resonances are detected in our study, which has historically been much harder to see than the E_{11L}^{M} resonance signal. For the $(10, 4)$ nanotube, laser energies were available to carry out the resonance profile determination as discussed above, but with the $(13, 4)$ nanotube, due to the unavailability of appropriate excitation sources, it was not possible to obtain a resonant profile to compare with theory. As can be

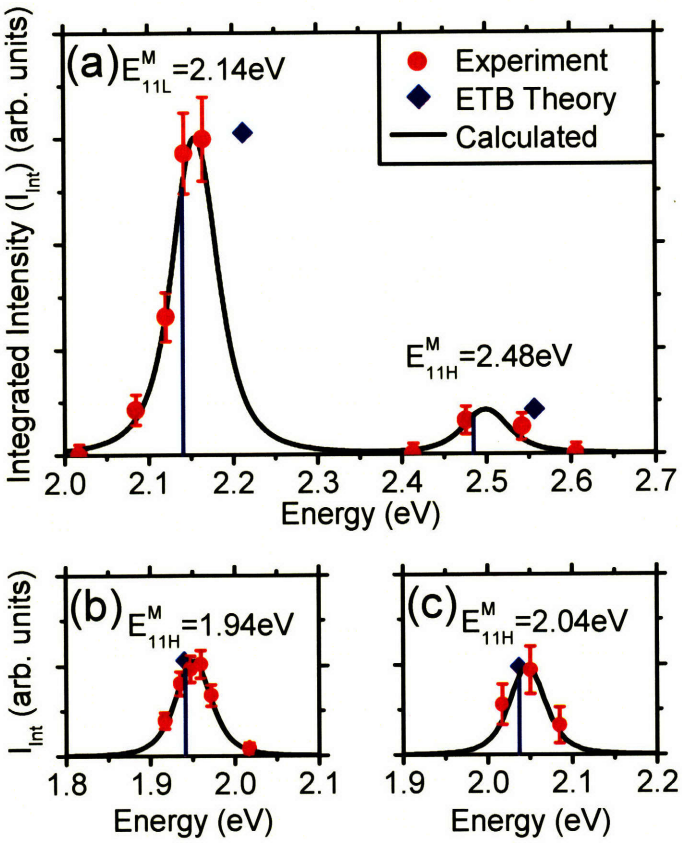

Figure 4-3: The resonance profile for (a) a (10,4) SWNT, (b) a (18,0) SWNT, and (c) a (15,3) SWNT. The red circles are the experimental integrated RBM intensities. The SWNT intensities were calibrated against that of the 520cm^{-1} Si peak. The blue diamonds are calculations using ETB+MB theory, and their horizontal positions correspond to the resonance energy. Regarding the intensity of the (10,4) SWNT, if the $E^{\mathrm{M}}_{11\mathrm{L}}$ and $E^{\mathrm{M}}_{11\mathrm{H}}$ results are matched, the experimental and theoretical results agree well (see text). The black line is the calculated RBM resonance profile using Eq. 4.1. The blue drop lines indicate the $E^{\mathrm{M}}_{11\mathrm{L}}$ and $E^{\mathrm{M}}_{11\mathrm{H}}$ values used for the calculated resonance profile. Note that the $E^{\mathrm{M}}_{11\mathrm{L}}$ and $E^{\mathrm{M}}_{11\mathrm{H}}$ differ from the peak center by $E_{\mathrm{ph}}/2$ for the Stokes process. The experimental points are downshifted by 72meV from the theoretical predictions for the (10,4) SWNT. All SWNTs show Γ=35meV.

seen from the table, the energies at E^{M}_{11H} match well with the ETB+MB calculations for all the data points, which are indicated by yellow diamonds in the Kataura plot in Fig. 4-1.

Table 4.1: The comparison of E^{M}_{11L} and E^{M}_{11H} transition energies between theory and experiment for metallic SWNTs.

		ETB+MB Theory		Experiment	
n	m	E^{M}_{11L}(eV)	E^{M}_{11H}(eV)	E^{M}_{11L}(eV)	E^{M}_{11H}(eV)
10	4	2.21	2.56	2.14 ± 0.02	2.48 ± 0.07
13	4	1.92	2.18	1.95 ± 0.07	2.16 ± 0.07
15	3	1.81	2.05	-	2.04 ± 0.02
14	5	1.81	1.99	-	2.00 ± 0.07
18	0	1.70	1.94	1.655	1.94 ± 0.02

It was surprising that our ETB theory predictions based on non-interacting electrons and matrix elements that do not include excitonic effects explicitly can reproduce the experimental intensity so well for the $(10, 4)$ SWNT presented in this chapter.

4.4 Conclusion

In summary, the observation of the optical transition corresponding to E^{M}_{11H} for metallic SWNTs is presented. The integrated RBM intensities associated for the E^{M}_{11H} transitions are much lower than for E^{M}_{11L} transitions and the observed intensities conform to predictions of ETB theory. A good signal to noise ratio is required to observe the weak E^{M}_{11H} transitions. A strong enough signal could be obtained by taking the Raman spectrum of individual SWNTs with a high efficiency confocal micro Raman system. The observation of E^{M}_{11L} and E^{M}_{11H} transitions from the same SWNT further validates ETB theory. The experimental method presented in this work allows an experimental determination of the magnitude of the electron-phonon coupling matrix elements for individual SWNTs.[46, 47]

Chapter 5

Strained Single Wall Carbon Nanotube

Strain in materials plays a very important role in tuning material properties. The best example is the strained-Si MOSFETs in nowadays' high-performance microprocessors which possess higher mobility in the channel due to the presence of the strain. Being a one dimensional system, it is predicted that strain can dramatically modify the electronic and optical properties of SWNTs.[48] Thus, strain is envisioned as a method for tuning the electronic and optical properties of SWNTs for device applications.[48, 49] However, most of the investigations have relied on manual manipulations to introduce strains in the SWNTs and have observed only axial strain.[50, 51]

In this chapter, a method of characterizing a continuously varying strain in individual SWNTs is reported. Using resonant Raman spectroscopy, the relationship between strain and the electronic and vibrational properties of the nanotube can be directly confirmed. Different types of strain, such as axial elongation or radial twisting (torsional strain) can be distinguished from the variations on different modes of SWNTs Raman spectra. More importantly, it is demonstrated that Raman spectroscopy can not only provide a confirmation for the effect of the strains on the properties of nanotubes, as what has been shown before, but can also serve as a powerful tool to image the profile of strains along the nanotube structure. The details of the work presented in the following sections can be found in Refs. [52, 53].

5.1 The Role of the Van Der Waals Interaction between Single Wall Carbon Nanotubes and the Substrate

Non-polar molecules such as SWNTs or single-layer graphene are bound to the substrate by a van der Waals (vdW) interaction with a certain amount of binding energy.[54] For SWNTs of 1nm diameter on a Si substrate, the binding energy per unit length is about 2eV/nm.[54] With this large amount of binding energy, the van der Waals interaction can cause significant friction when the structure is dragged on the surface of the substrate. This is the case when the SWNT is pulled by a tensile force, where friction will resist the movement of the SWNT, and axial strain will develop along the length of the nanotube. If one plots the strain versus the position along the SWNT, the slope of this strain profile will be proportional to the friction. In the simplest scenario where the friction is constant, the strain along the SWNT will vary linearly with the position (see Fig. 5-1(a)). The strain along the SWNTs would follow the relation:

$$\varepsilon = \frac{T}{A \times Y} = \frac{F_{tensile} - f \cdot x}{A \times Y}, \tag{5.1}$$

where ε is the axial strain at position x along the nanotube and $x = 0$ is the point where the tensile force $F_{tensile}$ is applied. T is the tension in the SWNT. $F_{tensile}$ is the pulling force on the nanotube. f is defined as the friction force between a SWNT and the substrate per unit length and Y is the Young's modulus of the SWNT, which is 1TPa. A is the cross sectional area of the SWNTs, which is 0.34 nm times the circumference of the SWNT. When $F_{tensile}$ is removed, the elastic retraction of the nanotube in combination with the friction will result in the triangular strain profile, as shown in Fig. 5-1(b).

The vdW interaction can also generate a tensile strain in SWNTs bound to a substrate. Line ABC in Fig. 5-2 shows a molecular wire contacting a substrate with an angle α. Assume that the wire is inelastic so that we can exclude elastic energy

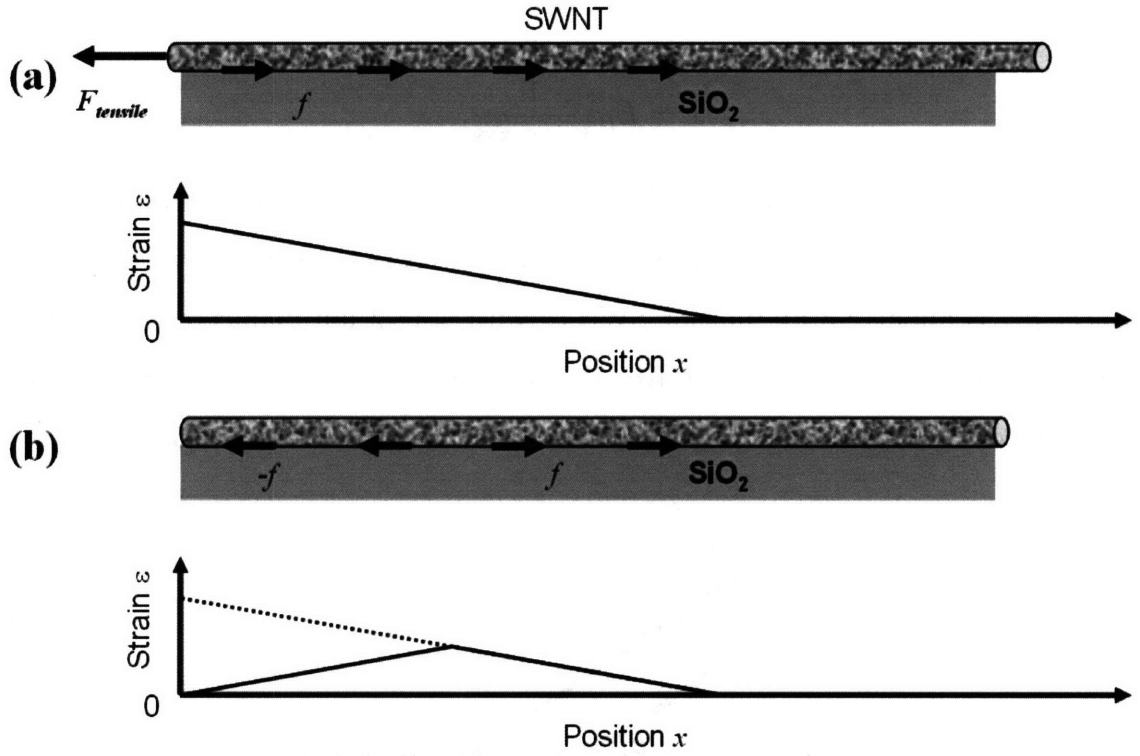

Figure 5-1: The strain versus position in the presence of a constant friction force between a SWNT and the substrate. (a) shows the strain profile when an external force is applied. (b) shows the strain profile after the external force is removed.

for simplicity. If the wire in the initial form ($\overline{ABC}$) is pulled from one end (point A) to the final form ($\overline{A'B'C}$) while keeping the contact angle constant, the work done in this process must be equal to the change in the total binding energy:

$$T(1-\cos\alpha)dx = E_B dx, \tag{5.2}$$

where E_B is the binding energy per unit length, dx is the length of $\overline{BB'}$, T is the tension of the wire. Thus,

$$T = E_B \frac{1}{1-\cos\alpha}. \tag{5.3}$$

At a small angle α, T has a much larger value than E_B, thereby possibly introducing a large strain into the molecular wire. For SWNTs on a H-passivated Si(100) surface, E_B is about 2-3 eV/nm for SWNTs with a 1~2 nm diameter.[54] As long as the surface is not chemically active, E_B on a different surface is expected to be similar since the Hamaker constants for different materials are similar.[55]

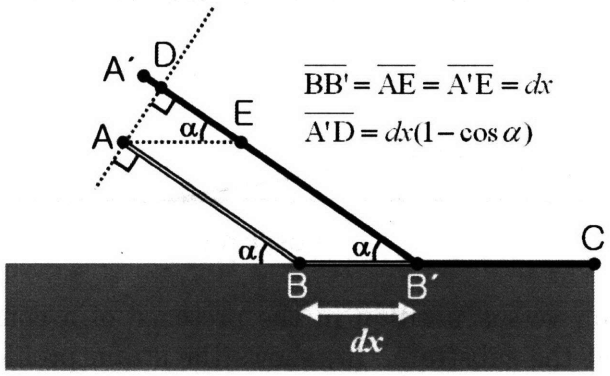

Figure 5-2: Molecular wire making contact with a substrate at an angle α. The wire in the initial form $\overline{ABC}$ is pulled by a force T to the final form $\overline{A'B'C}$. The vdW binding energy E_B between the substrate and the wire can sustain the tension in the wire.

5.2 Van Der Waals Interaction Induced Strain in Single Wall Carbon Nanotubes

To introduce strain into individual SWNTs using the vdW interaction, we used a silicon substrate with 300 nm-deep trenches with different widths: 1.5 μm, 3 μm and 6 μm. The trenches were patterned on a 300 nm silicon oxide film by dry etching. Well-separated ultra-long aligned SWNTs were grown across the trenches using an ethanol chemical vapor deposition method at 900°C. Figure 5-3(a) shows a scanning electron microscope (SEM) image of the SWNTs grown on the substrate. Figure 5-3(b) is an atomic force microscope (AFM) image of a single SWNT grown across the trenches (dark). From the AFM and SEM images, we found that the SWNTs often touch the bottom of the 6 μm-wide trenches, but rarely the bottom of narrower trenches [Fig. 5-3(b)]. Since the SWNTs are contacting the trench bottom with a certain angle, like in Fig. 5-2, it is expected that strain will develop in these SWNTs. There are various types of perturbations that can cause the SWNTs to touch the bottom of the trenches. In general, it appears that the wider the trench, the more frequent that the SWNT falls down to the bottom.

RRS was employed to characterize the vibrational modes of a SWNT along its length. A micro-Raman setup in a backscattering geometry with a 50× objective (numerical aperature=0.8) is used for collecting spectra with laser excitation wavelengths of 514 nm, 621 nm, 633 nm and 647 nm. The laser spot size is about 1 μm^2. Using an automated stage, Raman spectra are taken over the region near the trenches. Spectra are taken at two different laser power levels (0.9 mW and 3 mW) to ensure there is no heating effect. By plotting the integrated peak intensity of a vibrational mode in a two-dimensional (2-D) map, we can construct an image of the SWNT. Figure 5-4(b) shows such an image constructed from the G-band between 1500 cm^{-1} and 1600 cm^{-1}, where the color bar shows the intensity scale. Figure 5-4 shows the intensity map of the silicon peak at 520 cm^{-1} taken in the same region as Fig. 5-4(b), which identifies the trench regions. The 6 μm trench is at position y = 8 - 14 μm and is not shown in Fig. 5-4, since no SWNT Raman signal could be

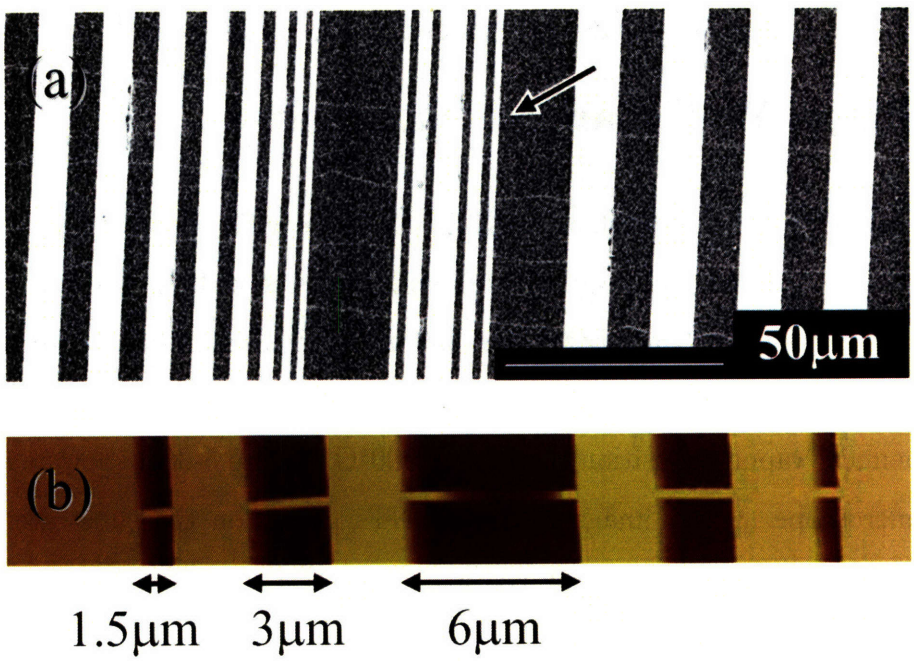

Figure 5-3: Generation of uniaxial strain using a patterned substrate. (a) The trench pattern used for the experiment. Light color represents the trenches patterned on a Si/SiO_2 substrate. (b) An AFM height image of a SWNT crossing multiple trenches in the center of (a). Dark color represents lower height.

obtained from the region where the SWNT touches the bottom of the 6 μm trench, probably due to the reduced electric field at the silicon surface. Based on the result of Fig. 5-4(b), we plot the Raman spectra of the G-band along the length of the SWNT. The frequency of the most intense peak (assigned to the A-symmetry mode of G^+) is marked by the red dashed line in Fig. 5-4(c). A downshift in this frequency as y increases from y = -4 μm can be clearly seen.

We observed five semiconducting SWNTs (S-SWNTs) with total frequency downshifts of 3-8 cm^{-1} and three other S-SWNTs with total frequency downshifts of 20 cm^{-1}, 54 cm^{-1}, 80 cm^{-1}, which are shown as blue squares, black triangles and red diamonds, respectively, in Fig. 5-5(b) . For each SWNT, the G-band frequency starts between 1590 and 1600 cm^{-1} in the left (y = -8 μm) and it stays constant to a point (indicated by arrows in Fig. 5-5(b)), where it suddenly starts downshifting linearly with respect to y. Except in the trench regions, this linear frequency shift behavior continues to the trench where the strain originates from.

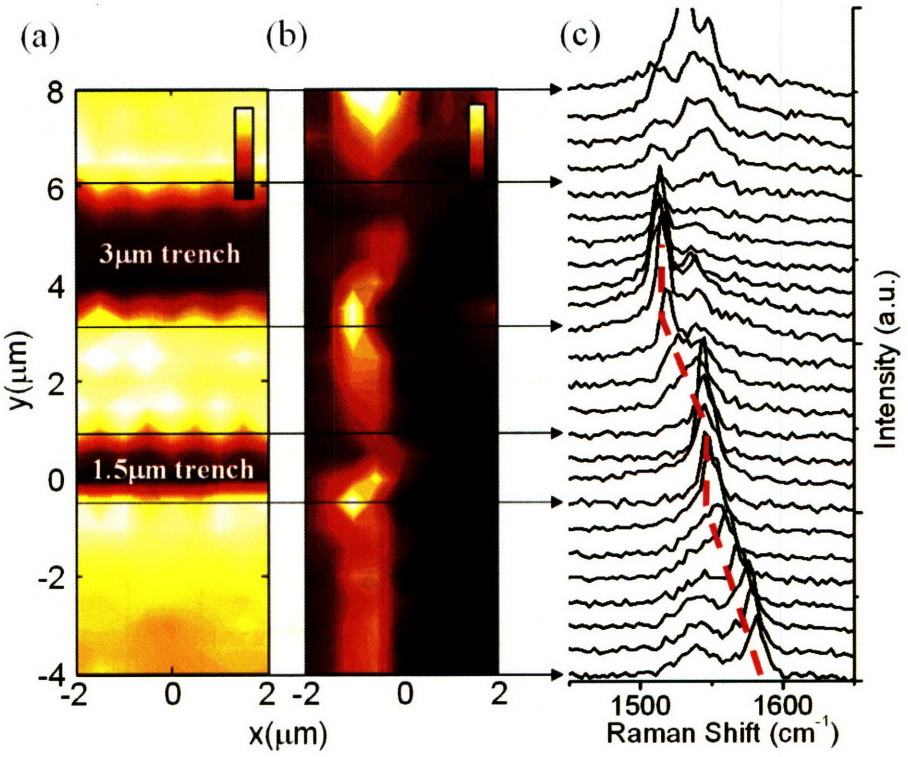

Figure 5-4: (a) 2D integrated intensity map of the silicon peak at 520 cm^{-1}. The dark regions correspond to the trench regions. (b) 2D integrated intensity map of the G band between 1500 and 1600 cm^{-1} taken from a SWNT in the same region as in (a). (c) Actual G-band spectra along the length of the SWNT shown in (b). The peak frequency of the most intense peak is observed to shift linearly with respect to the position on the substrate and remains constant across the trenches (see Fig. 5-5).

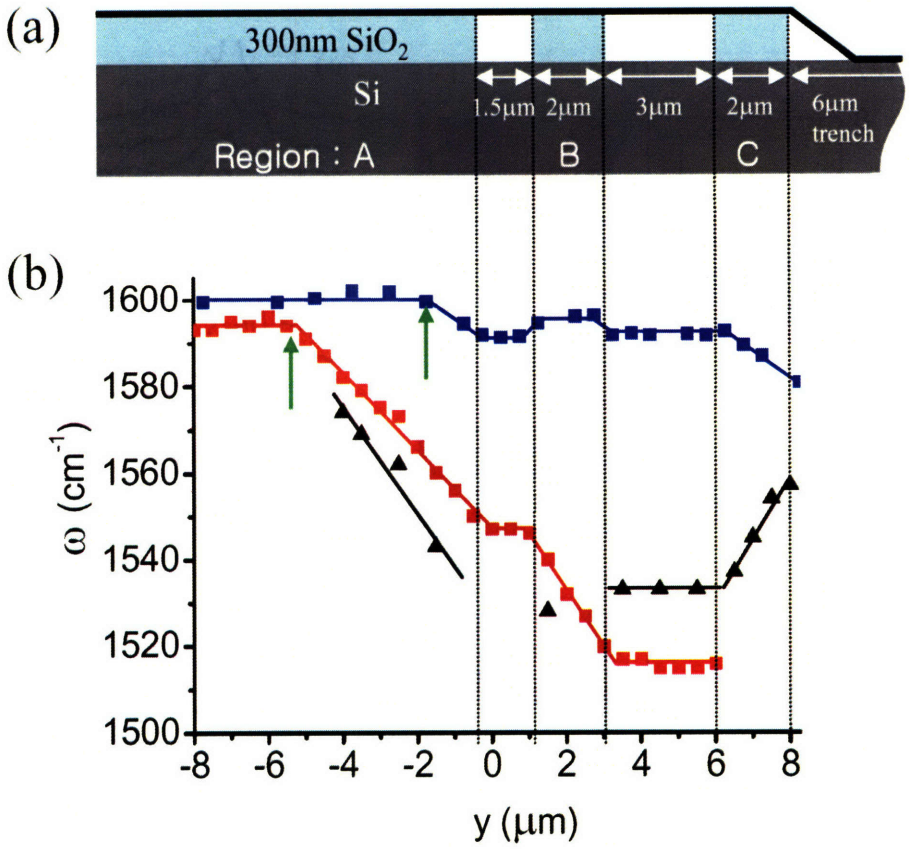

Figure 5-5: (a) A schematic of a SWNT crossing multiple trenches patterned on a Si/SiO_2 substrate. (b) G-band frequency obtained from Raman spectroscopy versus position for several SWNTs. The horizontal axis in (b) corresponds to the horizontal axis shown in (a). The G-band frequency is downshifted by up to $80cm^{-1}$, indicating that there is a large axial strain in the measured SWNTs.

The initial frequency between 1590 and 1600 cm^{-1} corresponds to the frequency of the A-symmetry mode of the G^+-band (ω_{G^+}) in unstrained semiconducting SWNTs. It is also reported that the G^+ feature downshifts linearly with respect to the axial strain of up to 1.6% strain in semiconducting SWNTs[50, 56]:

$$\omega_{G^+}(\varepsilon) = \omega_{G^+}(0) - k\varepsilon, \tag{5.4}$$

where ε is the axial strain and the measured value of k ranges from 6.8 to 28 cm^{-1} per 1% axial strain. Due to the experimental limitations in Refs. [50, 56], the measured values of k shall be taken as a lower limit of the true value of k.[50] Thus, we will take $k \geq 28$ cm^{-1} per 1% axial strain for all following analysis.

The observed frequency shift in Fig. 5-5 can be explained by the following model. The axial strain is generated at a trench (in most cases the 6 μm trench) according to Eq. 5.3 and it propagates along the SWNT until it relaxes to zero due to the friction between the SWNT and the substrate according to Eq. 5.1. As mentioned in the previous section, the linear frequency shift behavior indicates that f is constant along the length of each SWNT. Using Eqs. 5.1 and 5.4 and the measured slope from Fig. 5-5(b), we find that f is about 5pN/nm for SWNTs sitting on a SiO_2 substrate, which is about an order of magnitude higher per carbon atom than values reported for wall to wall interaction in double wall carbon nanotubes and multi wall carbon nanotubes.[57, 58]

To verify that the vdW interaction is sufficient to induce the observed strain, we have estimated the strain using the previously reported E_B.[54] From the SEM and AFM images, we measure the angle for different SWNTs on the sample, which ranges from about 8.5° to 30°. We calculate the maximum strain based on the tension using Eq. 5.3:

$$\varepsilon = \frac{T}{A \times Y} = \frac{E_B}{A \times Y} \times \frac{1}{1 - \cos\theta}. \tag{5.5}$$

The resulting strain ranges from a negligible value (less than 0.2%) to more than 3%, which is consistent with values observed in our study. Note that although the

vdW interaction is universal, supporting such a large strain solely by the vdW interaction is possible only in structures with nanometer thickness. In a general ribbon-like structure bound to a substrate, E_B is roughly proportional to the ribbon width, whereas the cross sectional area is proportional to the ribbon width times the thickness of the structure. Thus, the strain is expected to be inversely proportional to the thickness of the structure.

The large variation of the strain observed in different individual SWNTs is mostly due to the variation in the contact angle α but not to the variation in E_B. This is most likely due to randomness in the amount of slack in the SWNTs. Therefore, a better engineered trench profile and an improved process for the SWNT to fall down in a trench in a more controlled way would significantly reduce this randomness, making the method more useful for introducing a uniform strain on a large scale.

5.3 AFM Manipulation Induced Strain in Single Wall Carbon Nanotubes

In this section, using AFM manipulation, both uniaxial and torsional strain has been induced into individual, ultra-long oriented SWNTs. Raman spectra are obtained along the length of the SWNTs to constitute Raman images of the SWNTs. These images show that the vibrational modes have continuously varying frequencies along the length of the SWNTs and these frequency profiles have regular patterns. The pattern shows that there exist two types of strain in SWNTs after AFM manipulation, specifically uniaxial and torsional strain, and also that the strain propagation on a substrate is governed by the friction between the SWNT and the substrate, which is induced by the vdW interaction, as described in Section 5.1. The torsional strain has also caused peak splitting for some vibrational modes due to symmetry breaking effects. The Raman intensity variation shows that both uniaxial and torsional strain modulates the electronic transition energies of SWNTs. As predicted from the force analysis and also proved by the Raman results, the total amount of induced strains was dependent on the magnitude of the tensile force or torsional moment exerted on the SWNTs. The propagation or distribution of strains along the tube axis was determined by the friction between SWNTs and the substrate.

The SWNTs used for the AFM manipulation were grown by ethanol chemical vapor deposition directly on a silicon substrate with a 1 μm-thick oxide layer and the SWNTs have typical length of several millimeters. All the SWNTs are straight and oriented by the gas flow (similar to Fig. 5-3(a)). The AFM manipulation was performed along a predefined path nearly perpendicular to the SWNTs axis at the point which was millimeters away from the two ends. Figure 5-6 shows the AFM images of an ultra-long SWNT before and after the AFM manipulation. In most cases, the section of the SWNT near the manipulation point is pushed sideways and the SWNT is cut after manipulation as shown in Fig. 5-6(b).

The schematic figures of the AFM manipulation on the ultra-long, oriented SWNTs are shown in Fig. 5-7. As shown in Fig. 5-7(b), under the AFM manipulation, the

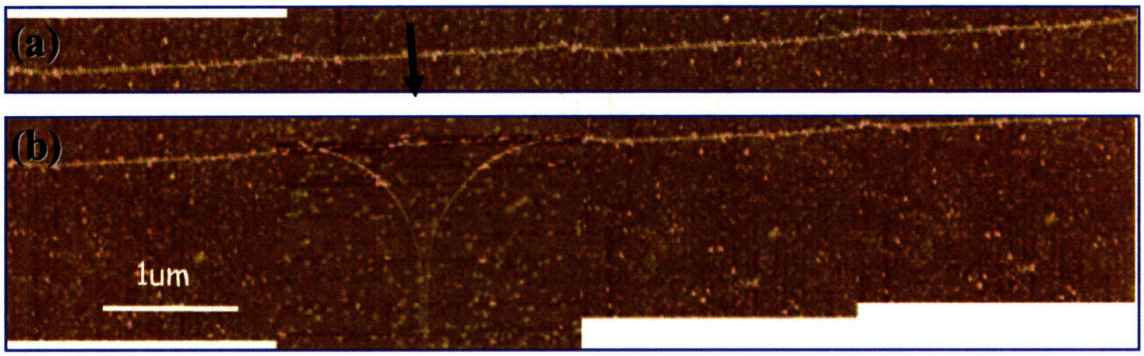

Figure 5-6: AFM images of an ultra-long SWNT before and after the AFM manipulation. (a) The AFM image of the SWNT before the AFM manipulation. The black arrow indicates the direction of AFM tip movement during the AFM manipulation. (b) The AFM image of the SWNT shown in (a) after the AFM manipulation.

contact point between the tube and tip was always above the center of the SWNT. Thus, the pushing force F combining the friction f between the SWNT and the substrate would induce a torsional moment in the SWNT cross section plane. And a simultaneous sliding and rolling movement could be caused by F and the torsional moment. Thus, in addition to the uniaxial strain generated by the elongation of the SWNT, as shown in Fig. 5-7(a), the AFM manipulation described above can induce a torsional strain in SWNTs.

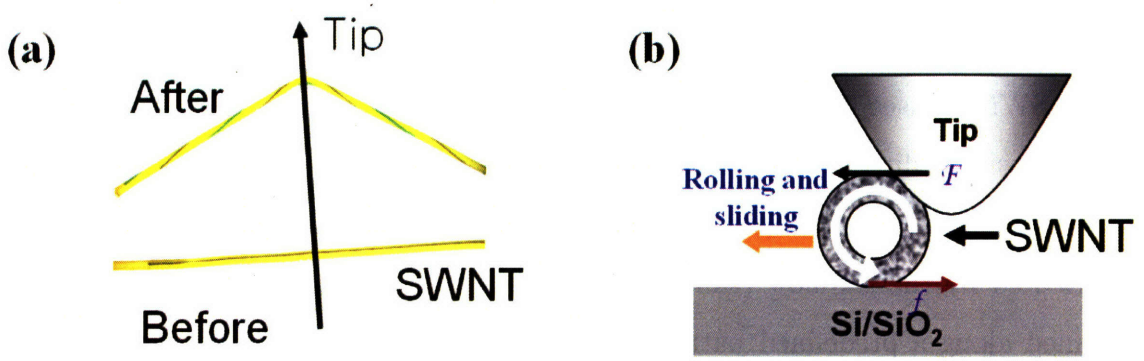

Figure 5-7: Generation of strain using AFM manipulation. (a) A schematic of the AFM manipulation causing both elongation and rotation of the SWNT under manipulation. (b) A schematic of the AFM manipulation causing rotation of the SWNT.

The theory behind the spatial propagation of the uniaxial strain is described in Section 5.1. This theory predicts that the strain profile for the uniaxial strain caused

by the AFM manipulation should be triangular near the manipulation point, as shown in Fig. 5-1. For the torsional strain, if we replace the $F_{tensile}$ with the applied torsional moment M_e, the Young's modulus Y with the graphene in-plane shear modulus G, the uniaxial strain ε with the torsional strain γ (equivalent to the shearing strain in a graphene sheet) in Eq. 5.1, a similar relation can be obtained:

$$\gamma = \frac{M_e/r - f_r \cdot x}{A \times G}, \tag{5.6}$$

where r is the radius of the SWNT and f_r is the component of friction force between the SWNT and the substrate that is perpendicular to the SWNT axis. Thus, the strain profile for the torsional strain after the AFM manipulation should also be triangular near the manipulation point, as shown in Fig. 5-1.

Note that, although the propagation of the uniaxial strain and the torsional strain are governed by similar physics, the values of the physical constants involved are different. Thus, the exact shape of the strain profile for the uniaxial strain and the torsional strain will be different.

The resonant micro-Raman spectra were obtained along the ultra-long SWNTs axis using a 632.8 nm He-Ne laser. The laser polarization was parallel to the tube axis. The excitation spot size was about 1$\sim$2 μm and the laser power was 8 mW/μm^2. All the Raman spectra were fitted to Lorentzian peak shapes to obtain the peak frequency and intensity. Figures 5-8 and 5-9 show the RBM frequency (ω_{RBM}) and G-band frequency profiles versus the position obtained from two representative SWNTs after the AFM manipulation.

The common features of the AFM manipulated SWNTs are shown in Fig. 5-8. Here we see that ω_{RBM} upshifts near the manipulation point and the pattern of the upshift has a "Λ" shape. One of the G-band modes, which is assigned to the E_2-symmetry mode of G^+ in Ref. [20], downshifts and the pattern of the downshift is a "V" shape. The regions where ω_{RBM} upshifts and where the E_2-symmetry mode of G^+ downshifts are always the same, which implies that these changes are due to a common factor.

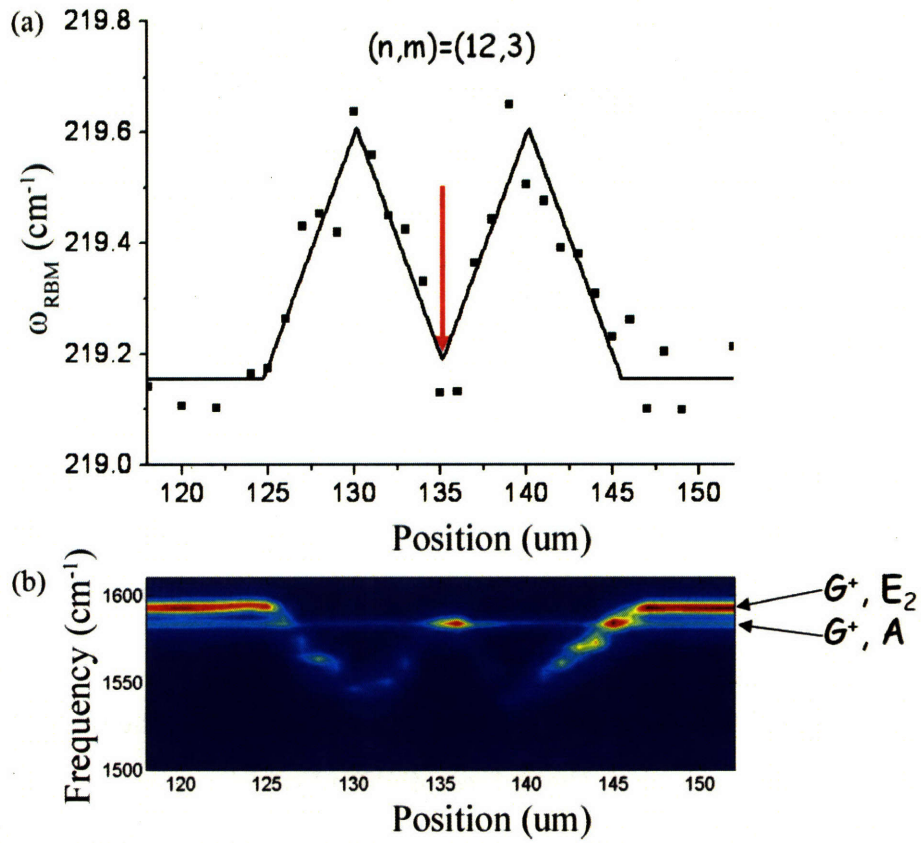

Figure 5-8: (a) The RBM frequency versus the SWNT position for a (12,3) SWNT after the AFM manipulation. The manipulation point is indicated by the red arrow. (b) The G-band region of the Raman spectra versus the SWNT position after the AFM manipulation. The arrows on the right indicate the E_2-symmetry mode and the A-symmetry mode of G^+.

Figure 5-9 shows an additional feature that is not shown in Fig. 5-8. Here we see that the A-symmetry mode of G^+ downshifts and the region where it downshifts is different from where ω_{RBM} upshifts. Thus, one can conclude that the downshift of the A-symmetry mode of G^+ is caused by another factor other than what is causing both the upshift of ω_{RBM} and the downshift of the E_2-symmetry mode of G^+.

To identify the factors that cause these changes, all known factors that can cause the changes in the Raman spectra will be listed and factors that cannot cause the Raman shift patterns described above will be eliminated. The factors which may influence the SWNT Raman spectra include temperature, charge transfer from underlying or surrounding substance, the interaction between the SWNT and the substrate, and

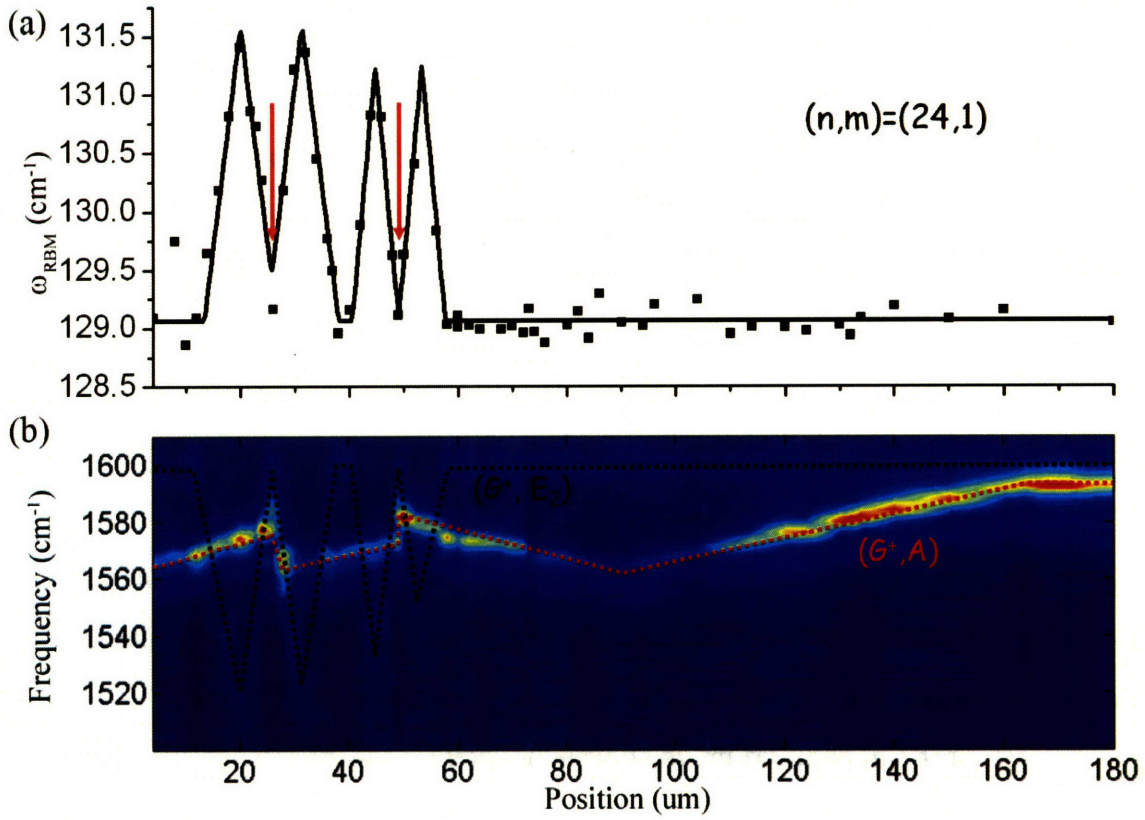

Figure 5-9: (a) The RBM frequency versus the SWNT position for a (24,1) SWNT after the AFM manipulation. The manipulation point is indicated by the red arrow. (b) The G-band region of the Raman spectra versus the SWNT position after the AFM manipulation. The black dotted line and the red dotted line denote the E_2-symmetry mode and the A-symmetry mode of G^+, respectively.

the SWNT deformation - uniaxial stretch or compression, torsion, bending and radial compression. Due to the good thermal contact between the SWNT and the substrate, no significant heating of the SWNT from the laser happened and there was no difference in the thermal contact before and after manipulation. So the temperature is not the factor causing the above Raman results. The charge transfer and the change in the SWNT/substrate interaction could not account for the Raman shift either, because if they were the responsible mechanism, the distribution of the frequency shift $\Delta\omega$ should be monotonic and no "V" or "Λ" shape should occur. By the process of elimination, it is suggested that the factor responsible for our observations may be the SWNT's deformation and from the AFM image, the geometrical curvature resulting from the manipulation is located in a region only about 3∼4 μm long, which is far less than the region where the Raman frequency shifts occurred. The localization of this effect excludes the bending strain. For a similar reason, the possible radial compression of the SWNT caused by the pressing of the AFM tip on the SWNT could also be excluded.

So the factors accounting for the above Raman frequency shifts may be uniaxial and torsional strain. The uniaxial strain has been reported to have no influence on ω_{RBM} and to cause ω_G to downshift.[50] This has also been proved by our study of the SWNTs with pure uniaxial strain which was induced by the sticking of the SWNT to the trench bottom, as discussed in Section 5.2.

Thus, it can be concluded that the factor causing the downshift of the A-symmetry mode of G^+ is the uniaxial strain and the factor causing the upshift of ω_{RBM} and the downshift of the E_2-symmetry mode of G^+ is the torsional strain. The "V" or "Λ" shaped distribution of the frequency shift indicated that both strains have experienced a relaxation and were propagated linearly along the axes of the SWNTs, which is consistent with the analysis in Section 5.1.

It is predicted that both uniaxial and torsional strains modulate the electronic band structure of the SWNT.[48, 49] Especially, the electronic transition energy E_{ii} can be tuned up to 100 meV per 1% strain.[48, 49] Experimentally, it has been shown that the band-gap of a SWNT can be tuned by 35∼53 meV per 1% uniaxial strain.[51]

In the Raman spectra of individual SWNTs, the peak intensity is strongly dependent on the resonance between the incident laser and the transition between electronic states at van Hove singularities (vHSs), that is, the matching between the energy of the incident laser E_l and the electronic transition energy E_{ii}. If the laser energy E_l is fixed, the intensity variation would reflect the E_{ii} change.

From resonance Raman theory, the intensity ratio of anti-Stokes and Stokes spectra satisfies the following relation:[59]

$$\frac{I_{AS}}{I_S} = \frac{|(E_l - E_{ii} - i\Gamma)(E_l + E_{\rm ph} - E_{ii} - i\Gamma)|^2}{|(E_l - E_{ii} - i\Gamma)(E_l - E_{\rm ph} - E_{ii} - i\Gamma)|^2} \exp\left(-\frac{E_{ph}}{k_B T}\right). \tag{5.7}$$

Here, I_S and I_{AS} are the Stokes and the anti-Stokes intensities, respectively, E_{ph} is the phonon energy, and Γ gives the inverse lifetime of the intermediate electronic states. The last exponential factor in Eq. 5.7 is the Bose-Einstein thermal factor, where k_B is the Boltzmann constant and T is the temperature. It can be seen that for a fixed E_l, both I_S and I_{AS}/I_S are E_{ii} dependent and if the value of Γ could be determined, the E_{ii} could then be estimated from I_{AS}/I_S. In our system, setting Γ to 35 meV and T to 300K gave the best fit between the experimental and theoretical I_S and I_{AS}/I_S and those values have been used for the following E_{ii} analysis.

Figures 5-10(a) and 5-10(b) show the anti-Stokes to the Stokes intensity ratio I_{AS}/I_S of the RBM and the G-band region of the Raman spectra for the (24,1) SWNT shown in Fig. 5-9. Using Eq. 5.7, one can obtain the E_{ii} value as a function of position. The minimum and maximum E_{ii} values are about 1.92±0.015 eV at the position 165 μm and 2.00±0.015 eV at 90 μm, respectively. Using Eq. 5.4 and the frequency of the A-symmetry mode of the G^+ shown in Fig. 5-10(b), one can obtain the uniaxial strain as a function of position. The minimum and maximum uniaxial strains are 0 % at 165 μm and 1 % at 90 μm, respectively. Since the value of k used in Eq. 5.4 is a lower limit of the true value of k, the strain values calculated here are an upper limit of the actual value of strain. Assuming that the change in the E_{ii} value is proportional to the uniaxial strain [48, 49], one can obtain the E_{ii} value as a function of position as shown in Fig. 5-10(c). The calculated I_{AS}/I_S value using

this E_{ii} value and Eq. 5.7 matches the experimental I_{AS}/I_S value well as shown in 5-10(a). Thus, it can be concluded that the change in the E_{ii} value is proportional to the uniaxial strain and the proportionality constant is at least 80±20 meV per 1 % strain for this particular SWNT. This value is consistent with theoretical predictions and previous experimental measurements.[49, 51, 48]

It is predicted that, under torsional strain, symmetry breaking will cause mode splitting in the G-band.[60] Figure 5-11 shows the G-band region of the Raman spectra obtained from another AFM manipulated SWNT identified as (13,4). The original ω_{RBM} of this SWNT is 195.5 cm^{-1}. The shift in ω_{RBM} (denoted by $\Delta\omega_{\mathrm{RBM}}$) after the manipulation is used as a measure of the torsional strain. As the torsional strain increases, more peaks appear in the G-band region of the Raman spectra. When $\Delta\omega_{\mathrm{RBM}}$ reaches 1.6 cm^{-1} (maximum torsional strain), there are at least three additional peaks compared to when $\Delta\omega_{\mathrm{RBM}}$=0 (no torsional strain).

Since the G-band region shown in Fig. 5-11 shows a rich spectrum of peaks, the identification of these peaks to different symmetry modes of the G-band in a metallic SWNT would be an interesting future work. A previous work carried out polarization dependent Raman study to identify different symmetry modes of the G-band in a semiconducting SWNT [20], and a similar approach might be used to carry out this work. On the other hand, it was found that the response of certain modes to the torsional strain in a metallic SWNT is different from that in a semiconducting SWNT. Details of this difference are discussed in Ref. [53].

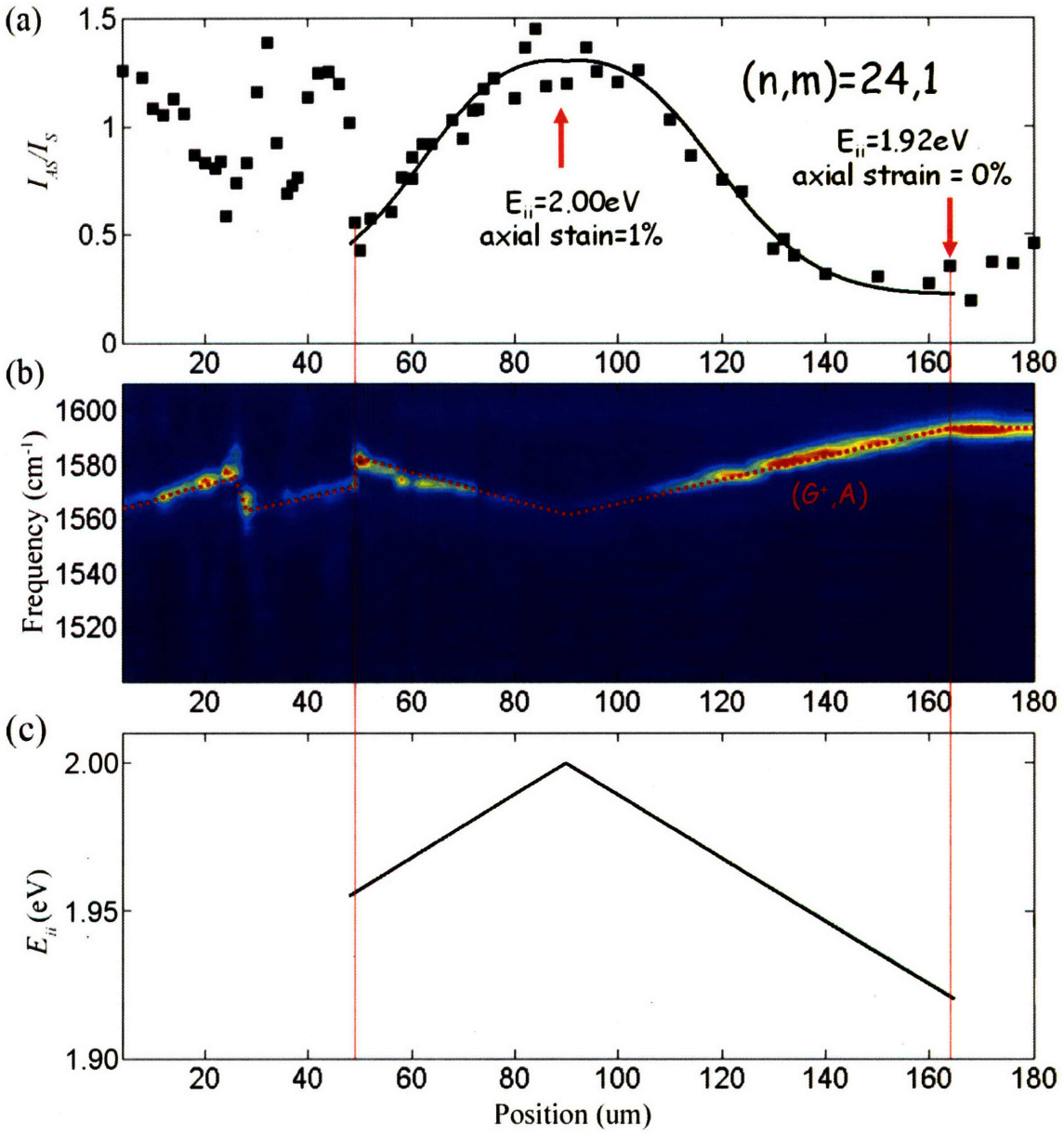

Figure 5-10: (a) The anti-Stokes to the Stokes intensity ratio I_{AS}/I_S of the RBM for the SWNT shown in Fig. 5-9. The black squares are the experimental data. The black line is the calculated intensity ratio using the E_{ii} value shown in (c). (b) The G-band region of the Raman spectra versus the position after the AFM manipulation. The red dotted line denote the A-symmetry mode of G^+. (c) The E_{ii} value as a function of position estimated from the anti-Stokes to the Stokes intensity ratio. The change in the E_{ii} value is proportional to the frequency shift in the A-symmetry mode of the G^+ shown in (b). The vertical lines are to guide the reader.

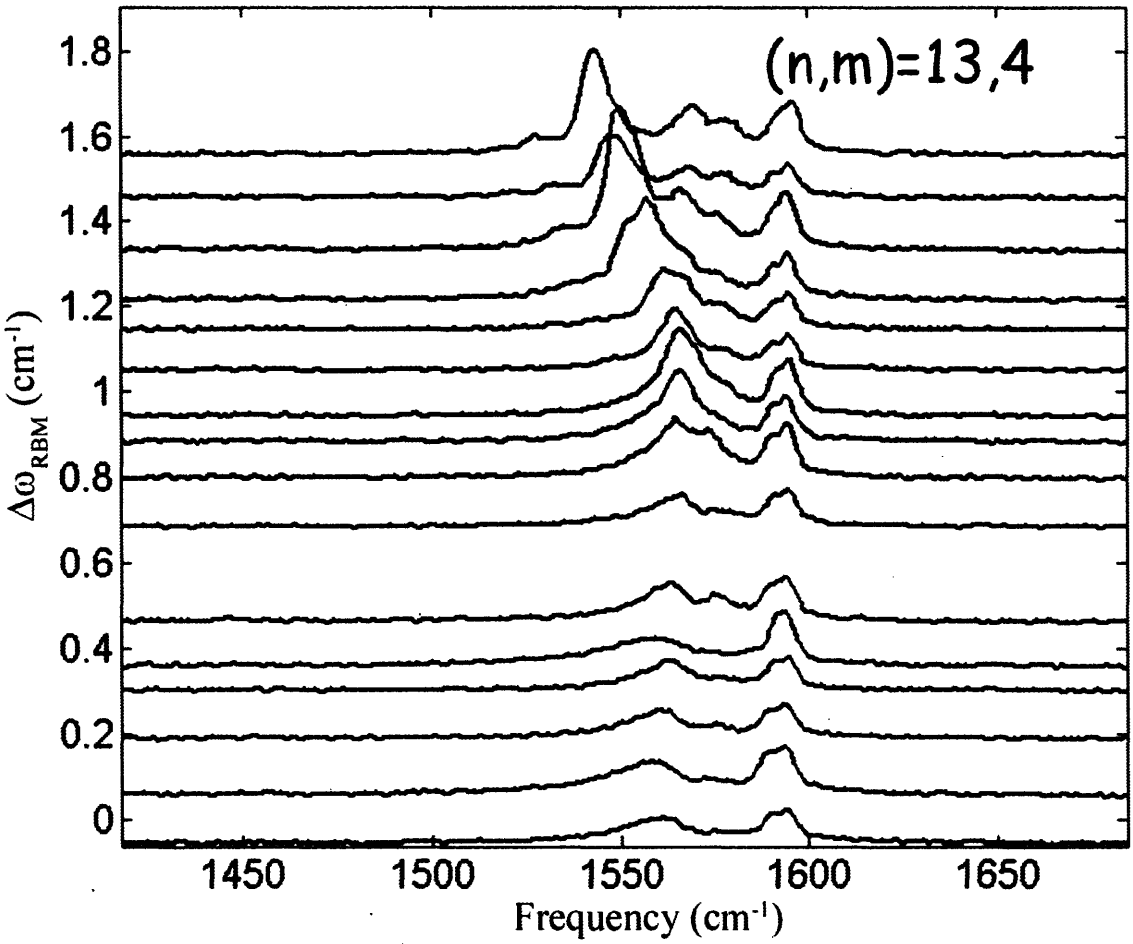

Figure 5-11: The G-band region of the Raman spectra obtained from an AFM manipulated SWNTs shown at different $\Delta\omega_{\mathrm{RBM}}$. Here $\Delta\omega_{\mathrm{RBM}}$ is used as a measure of the torsional strain. As $\Delta\omega_{\mathrm{RBM}}$ increases, more peak splitting can be found in the G-band region.

5.4 Conclusion

In summary, torsional and axial strain are introduced by atomic force microscopy manipulations. Torsional strain strongly affects the Raman spectra, inducing a large downshift in the frequency of the E_2-symmetry mode in the G^+ band, and a slight upshift in the frequency of the RBM. Whereas uniaxial strain has little effect on the frequency of the E_2-symmetry mode of the G^+ band and the RBM, it downshifts the frequency of the A-symmetry mode of the G^+ band. The uniaxial strain is shown to strongly affect the electronic transition energy E_{ii} of the SWNT. Finally, it is shown that torsional strain can cause mode splitting in the G-band in some SWNTs.

Chapter 6

Conclusion

First of all, one of the big challenges in SWNT research, the lack of a Raman instrument capable of obtaining Raman spectra efficiently with tunable laser excitation, is addressed. The design and construction of a high-efficiency widely-tunable Raman instrument for the study of SWNTs is reported. The use of such an instrument is not limited to the work described in this thesis. The instrument has been used to characterize the dependence of Raman spectra on the length of SWNTs [61, 62], to study phonon softening in metallic SWNTs [63], to characterize nitrogen doped SWNTs [64], and to characterize graphite foams [65]. At the time of writing, the instrument is being utilized in many other projects such as identifying the chirality distribution of SWNTs grown from a specific growth process [66], studying charge-induced changes in metallic SWNTs [67], obtaining Raman spectra from both the inner and outer walls of individual double wall carbon nanotubes [68], characterizing the quality of graphene films grown by a chemical vapor deposition method [69], and obtaining high signal-to-noise ratio Raman spectra from tissues for biomedical studies [70].

In Chapter 3, the environmental effects on the electronic and vibrational properties are investigated in suspended SWNTs. The enhanced signal and unperturbed environment in suspended SWNTs proved to be useful in later studies.[27, 28] In Chapter 4, using the high-efficiency Raman instrument, weak optical transitions of metallic SWNTs that was previously unreported in Raman studies are found. Finally, in Chapter 5, the effects of strain on the vibrational mode frequencies and the

electronic band structure of SWNTs are studied and the findings are consistent with previous theoretical predictions and experimental studies.

Bibliography

[1] R. Saito, G. Dresselhaus, and M. S. Dresselhaus, *Physical Properties of Carbon Nanotubes*, Imperial College Press, 1999.

[2] J. Lefebvre, Y. Homma, and P. Finnie, Phys. Rev. Lett. **90**, 217401 (2003).

[3] M. Y. Sfeir, T. Beetz, F. Wang, L. Huang, X. M. H. Huang, M. Huang, J. Hone, S. O'Brien, J. A. Misewich, T. F. Heinz, L. Wu, Y. Zhu, and L. E. Brus, Science **312**, 554 (2006).

[4] K. Balasubramanian, M. Burghard, K. Kern, M. Scolari, and A. Mews, Nano Letters **5**, 507 (2005).

[5] H. Kataura, Y. Kumazawa, Y. Maniwa, I. Umezu, S. Suzuki, Y. Ohtsuka, and Y. Achiba, Synth. Metals, 103, 2555 (1999).

[6] R. Saito, G. Dresselhaus, and M. S. Dresselhaus, Phys. Rev. B **61**, 2981 (2000).

[7] Ge. G. Samsonidze, R. Saito, N. Kobayashi, A. Grüneis, J. Jiang, A. Jorio, S. G. Chou, G. Dresselhaus, and M. S. Dresselhaus, Appl. Phys. Lett. **85**, 5703 (2004).

[8] P. Jarillo-Herrero, S. Sapmaz, C. Dekker, L. P. Kouwenhoven, and H. S. J. van der Zant, Nature **429**, 389 (2004).

[9] S. M. Bachilo, M. S. Strano, C. Kittrell, R. H. Hauge, R. E. Smalley, and R. B. Weisman, Science **298**, 2361 (2002).

[10] S. G. Chou, H. B. Ribeiro, E. Barros, A. P. Santos, D. Nezich, Ge. G. Samsonidze, C. Fantini, M. A. Pimenta, A. Jorio, F. Plentz Filho, M. S. Dresselhaus,

G. Dresselhaus, R. Saito, M. Zheng, G. B. Onoa, E. D. Semke, A. K. Swan, M. S. Ünlü, and B. B. Goldberg, Chem. Phys. Lett. **397**, 296 (2004).

[11] A. Jorio, R. Saito, J. H. Hafner, C. M. Lieber, M. Hunter, T. McClure, G. Dresselhaus, and M. S. Dresselhaus, Phys. Rev. Lett. **86**, 1118 (2001).

[12] R. Pfeiffer, H. Kuzmany, C. Schaman, T. Pichler, H. Kataura, Y. Achiba, J. Kürti, and V. Zólyomi, Phys. Rev. Lett. **90**, 225501 (2003).

[13] A. G. Souza Filho, S. G. Chou, Ge. G. Samsonidze, G. Dresselhaus, M. S. Dresselhaus, L. An, J. Liu, A. K. Swan, M. S. Ünlü, B. B. Goldberg, A. Jorio, A. Grüneis, and R. Saito, Phys. Rev. B **69**, 115428 (2004).

[14] C. Fantini, A. Jorio, M. Souza, M. S. Strano, M. S. Dresselhaus, and M. A. Pimenta, Phys. Rev. Lett. **93**, 147406 (2004).

[15] H. Son, Y. Hori, S. G. Chou, D. Nezich, Ge. G. Samsonidze, G. Dresselhaus, M. S. Dresselhaus, and E. Barros, Appl. Phys. Lett. **85**, 4744 (2004), November 29, 2004 issue of Virtual Journal of Nanoscale Science & Technology.

[16] T. Ono, H. Miyashita, and M. Esashi, Nanotechnology **13**, 62 (2002).

[17] Y. Zhang, A. Chang, J. Cao, Q. Wang, W. Kim, Y. Li, N. Morris, E. Yenilmez, J. Kong, and H. Dai, Appl. Phys. Lett. **79**, 19 (2001).

[18] J. Kong, H. T. Soh, A. M. Casswell, C. F. Quate, and H. Dai, Nature (London) **395**, 878 (1998).

[19] E. Joselevich and C. M. Lieber, Nano Lett. **2**, 10, 1137 (2002).

[20] A. Jorio, M. A. Pimenta, A. G. Souza Filho, Ge. G. Samsonidze, A. K. Swan, M. S. Ünlü, B. B. Goldberg, R. Saito, G. Dresselhaus, and M. S. Dresselhaus, Phys. Rev. Lett. **90**, 107403 (2003).

[21] M. S. Dresselhaus, G. Dresselhaus, A. Jorio, A. G. Souza Filho, and R. Saito, Carbon **40**, 2043 (2002).

[22] P. Corio, S. D. M. Brown, A. Marucci, M. A. Pimenta, , K. Kneipp, G. Dresselhaus, and M. S. Dresselhaus, Phys. Rev. B **61**, 13202 (2000).

[23] S. D. M. Brown, P. Corio, A. Marucci, M. A. Pimenta, M. S. Dresselhaus, and G. Dresselhaus, Phys. Rev. B **61**, 7734 (2000).

[24] L. Alvarez, A. Righi, T. Guillard, S. Rols, E. Anglaret, D. Laplaze, and J.-L. Sauvajol, Chem. Phys. Lett. **316**, 186 (2000).

[25] C. Fantini, A. Jorio, M. Souza, L. O. Ladeira, M. A. Pimenta, A. G. Souza Filho, R. Saito, Ge. G. Samsonidze, G. Dresselhaus, and M. S. Dresselhaus, Phys. Rev. Lett. **93**, 087401 (2004).

[26] U. J. Kim, X. M. Liu, C. A. Furtado, G. Chen, R. Saito, J. Jiang, M. S. Dresselhaus, and P. C. Eklund, Phys. Rev. Lett. **95**, 157402 (2005).

[27] K. Kaminska, J. Lefebvre, D. G. Austing, and P. Finnie, Nanotechnology **18**, 165707 (2007).

[28] E. Pop, D. Mann, J. Cao, Q. Wang, K. Goodson, and H. Dail, Phys. Rev. Lett. **95**, 155505 (2005).

[29] J. Maultzsch, H. Telg, S. Reich, and C. Thomsen, Phys. Rev. B **72**, 205438 (2005).

[30] M. J. O'Connell, S. Sivaram, and S. K. Doorn, Phys. Rev. B **69**, 235415 (2004).

[31] A. M. Rao, J. Chen, E. Richter, U. Schlecht, P. C. Eklund, R. C. Haddon, U. D. Venkateswaran, Y.-K. Kwon, and D. Tomanek, Phys. Rev. Lett. **86**, 3895 (2001).

[32] H. Son, A. Reina, Ge. G. Samsonidze, R. Saito, A. Jorio, M. S. Dresselhaus, and J. Kong, Phys. Rev. B **74**, 073406 (2006).

[33] J. Kong, H. T. Soh, A. M. Casswell, C. F. Quate, and H. Dai, Nature **395**, 878 (1998).

[34] Y. Yin, S. B. Cronin, A. G. Walsh, A. Stolyarov, M. Tinkham, A. N. Vamivakas, R. R. Bacsa, M. S. Unlu, B. B. Goldberg, A. K. Swan, and W. Bacsa, Proceedings of the Nanotechnology Conference and Trade Show, May (2005).

[35] L. X. Zheng, M. J. O'Connell, S. K. Doorn, X. Z. Liao, Y. H. Zhao, E. A. Akhadov, M. A. Hoffbauer, B. J. Roop, Q. X. Jia, R. C. Dye, D. E. Peterson, S. M. Huan, J. Liu, and Y. T. Zhu, Nature Materials **3**, 673 (2004).

[36] R. M. Martin and L. M. Falicov, *Light Scattering in Solids I: edited by M. Cardona*, volume 8, pages 79–145, Springer-Verlag, Berlin, 1983, Chapter 3, Topics in Applied Physics.

[37] J. Maultzsch, R. Pomraenke, S. Reich, E. Chang, D. Prezzi, A. Ruini, E. Molinari, M. S. Strano, C. Thomsen, and C. Lienau, Phys. Rev. B **72**, 241402(R) (2005).

[38] F. Wang, G. Dukovic, L. E. Brus, and T. F. Heinz, Science **308**, 838 (2005).

[39] J. Jiang, R. Saito, K. Sato, J. S. Park, Ge. G. Samsonidze, A. Jorio, G. Dresselhaus, and M. S. Dresselhaus, Phys. Rev. B **75**, 035405 (2007).

[40] A. Jorio, C. Fantini, M. A. Pimenta, R. B. Capaz, Ge. G. Samsonidze, G. Dresselhaus, M. S. Dresselhaus, J. Jiang, N. Kobayashi, A. Grüneis, and R. Saito, Phys. Rev. B **71**, 075401 (2005).

[41] A. Grüneis, R. Saito, Ge. G. Samsonidze, T. Kimura, M. A. Pimenta, A. Jorio, A. G. S. Filho, G. Dresselhaus, and M. S. Dresselhaus, Phys. Rev. B **67**, 165402 (2003).

[42] J. Jiang, R. Saito, Ge. G. Samsonidze, S. G. Chou, A. Jorio, G. Dresselhaus, and M. S. Dresselhaus, Phys. Rev. B **72**, 235408 (2005).

[43] S. B. Cronin, Y. Yin, A. Walsh, R. B. Capaz, A. Stolyarov, P. Tangney, M. L. Cohen, S. G. Louie, A. K. Swan, M. S. Ünlü, B. B. Goldberg, and M. Tinkham, Phys. Rev. Lett. **96**, 127403 (2006).

[44] C. Fantini, A. Jorio, M. Souza, M. S. Strano, M. S. Dresselhaus, and M. A. Pimenta, Phys. Rev. Lett. **93**, 147406 (2004).

[45] A. Jorio, A. G. Souza Filho, G. Dresselhaus, M. S. Dresselhaus, R. Saito, J. H. Hafner, C. M. Lieber, F. M. Matinaga, M. S. S. Dantas, and M. A. Pimenta, Phys. Rev. B **63**, 245416 (2001).

[46] A. G. Souza Filho, N. Kobayashi, J. Jiang, A. Grüneis, R. Saito, S. B. Cronin, J. Mendes Filho, Ge. G. Samsonidze, G. Dresselhaus, and M. S. Dresselhaus, Phys. Rev. Lett. **95**, 217403 (2005).

[47] J. Jiang, R. Saito, A. Grüneis, S. G. Chou, Ge. G. Samsonidze, A. Jorio, G. Dresselhaus, and M. S. Dresselhaus, Phys. Rev. B **71**, 205420 (2005).

[48] L. Yang and J. Han, Phys. Rev. Lett. **85**, 154 (2000).

[49] R. Hyed, A. Charlier, and E. McRae, Phys. Rev. B **55**, 6820 (1997).

[50] S. B. Cronin, A. K. Swan, M. S. Unlu, B. B. Goldberg, M. S. Dresselhaus, and M. Tinkham, Phys. Rev. Lett. **93**, 167401 (2004).

[51] E. D. Minot, Y. Yaish, V. Sazonova, J.-Y. Park, M. Brink, and P. L. McEuen, Phys. Rev. Lett. **90**, 156401 (2003).

[52] H. Son, Ge. G. Samsonidze, Y. Zhang, X. Duan, J. Zhang, Z. Liu, and M. Dresselhaus, Appl. Phys. Lett. **90**, 253113 (2007).

[53] X. Duan, H. Son, B. Gao, J. Zhang, T. Wu, Ge. G. Samsonidze, M. S. Dresselhaus, Z. Liu, and J. Kong, Nano Lett. **7**, 2116 (2007).

[54] T. Hertel, R. E. Walkup, and P. Avouris, Phys. Rev. B **58**, 13870 (1998).

[55] J. Israelachvili, *Intermolecular & Surface Forces*, Academic, London, 1994.

[56] S. B. Cronin, A. K. Swan, M. S. Unlu, B. B. Goldberg, M. S. Dresselhaus, and M. Tinkham, Phys. Rev. B **72**, 035425 (2005).

[57] J. Cumings and A. Zettl, Science **289**, 602 (2000).

[58] Y. Zhao, C. C. Ma, G. Chen, and Q. Jiang, Phys. Rev. Lett. **91**, 175504 (2004).

[59] A. G. Souza Filho, A. Jorio, J. H. Hafner, C. M. Lieber, R. Saito, M. A. Pimenta, G. Dresselhaus, and M. S. Dresselhaus, Phys. Rev. B **63**, 241404R (2001).

[60] G. Wu, J. Zhou, and J. Dong, Phys. Rev. B **72**, 115411 (2005).

[61] S. G. Chou, H. Son, J. Kong, A. Jorio, R. Saito, M. Zheng, G. Dresselhaus, and M. S. Dresselhaus, Appl. Phys. Lett. **90**, 131109 (2007).

[62] S. G. Chou, H. Son, M. Zheng, R. Saito, A. Jorio, G. Dresselhaus, and M. S. Dresselhaus, Chem. Phys. Lett. **443**, 328 (2007).

[63] H. Farhat, H. Son, Ge. G. Samsonidze, S. Reich, M. S. Dresselhaus, and J. Kong, Phys. Rev. Lett. **99**, 145506 (2007).

[64] F. Villalpando-Paez, A. Zamudioand, A. L. Elias, H. Son, E. B. Barros, S. G. Chou, Y. A. Kim, H. Muramatsu, T. Hayashi, J. Kong, H. Terrones, G. Dresselhaus, M. Endo, M. Terrones, and M. S. Dresselhaus, Chem. Phys. Lett. **424**, 345 (2007).

[65] E. B. Barros, H. Son, Ge. G. Samsonidze, A. G. S. Filho, J. M. Filho, G. Dresselhaus, and M. S. Dresselhaus, Phys. Rev. B **76**, 035444 (2007).

[66] Y. P. Hsieh, H. Son, M. Hofmann, C. T. Liang, Y. F. Chen, L. C. Chen, M. S. Dresselhaus, and J. Kong, (unpublished) .

[67] H. Farhat, M. Kalbac, H. Son, M. Dresselhaus, and J. Kong, (unpublished) .

[68] F. Villalpando-Paez, H. Son, A. Reina, J. Kong, Y. A. Kim, M. Endo, M. Terrones, and M. S. Dresselhaus, (unpublished) .

[69] A. Reina, X. Jia, H. Son, M. S. Dresselhaus, and J. Kong, (unpublished) .

[70] G. P. Singh, I. Barman, H. Son, R. R. Dasari, and M. S. Feld, (unpublished) .